Magnon scattering off quantum Hall skyrmion crystals probes interplay of topology and symmetry breaking

Nilotpal Chakraborty [1,*] Roderich Moessner,[1] and Benoit Doucot[2]

[1]*Max-Planck-Institut für Physik komplexer Systeme, Nöthnitzer Straße 38, Dresden 01187, Germany*
[2]*LPTHE, UMR 7589, CNRS and Sorbonne Université, 75252 Paris Cedex 05, France*

We introduce a model to study magnon scattering in skyrmion crystals, sandwiched between ferromagnets, which act as the source of magnons. Thanks to recent experimental advances, such a set-up can be realised in quantum Hall heterojunctions, and it is interesting as skyrmions are topological objects while the skyrmion crystals break internal and translational symmetries, thus allowing to study the interplay of topological and symmetry breaking physics. Starting from a basis of holomorphic theta functions, we construct an appropriate analytical ansatz for such a junction with finite spatially modulating topological charge density in the central region and vanishing in the leads. We then construct a suitably defined energy functional for the junction in terms of these spinors and derive the resulting equations of motion, which take the form of a Bogoliubov-de Gennes-like equation. Using a combination of analytical techniques, field theory, heuristic models, and fully microscopic recursive transfer-matrix numerics, we calculate the spectra and magnon transmission properties of the skyrmion crystal. We find that magnon transmission can be understood via a combination of low-energy Goldstone modes and effective emergent Landau levels at higher energies. The presence of the former manifests in discrete low-energy peaks in the transmission spectrum and we show how the these features reflect the nature of the Goldstone modes arising from symmetry breaking. In turn, the effective Landau levels, which reflect the topology of the skyrmion crystal, lead to band-like transmission features, from the structure of which further details of the excitation spectrum of the skyrmion crystal can be inferred. Such characteristic transmission features are not present in competing phases of either the quantum Hall phase diagram or in metallic magnets, and hence provide direct and unique signatures of skyrmion crystal phases and their properties. We discuss experimental considerations regarding the realisation of our model, which most directly apply to heterojunctions in monolayer graphene with the central region doped slightly away from unit filling and the two ends exactly at unit filling, a $\nu = 1 : 1 \pm \delta\nu : 1$ junction. Such physics is also relevant to junctions formed by metallic magnets, which host skyrmion crystal phases, or partly in junctions with artificially realized and periodically modulated gauge fields.

I. INTRODUCTION

Two central paradigms of condensed matter physics are symmetry breaking and, more recently, topology [1,2]. The concepts involved, down to the language describing them, are quite distinct, and it is interesting to ask what happens in "mixed situations" where emergent topology and symmetry breaking are both present. One of these is provided by the physics of skyrmions, which are topological objects, which also carry a notion of symmetry breaking—most immediately regarding internal spin degree of freedom. Natural questions thus arise regarding the demands of the respective paradigms. For instance, Goldstone's theorem demands the existence of stable quasiparticles, low energies, while topological phases

tend to come with gapped spectra and low-lying excitations living only at edges and interfaces. Moreover, the natural excitations of topological systems can have quantum numbers, which are quite distinct from those of the underlying electronic degrees of freedom.

A case in point is the SU(2)-invariant quantum Hall effect at $\nu = 1$, where a quantized transport plateau coexists with skyrmionic elementary excitations arising from the ferromagnetic ground state. Quantum Hall skyrmions are special in that they possess quantized electrical charge [3]. Tuning slightly away from this filling is believed to lead to the formation of a ground-state configuration of skyrmion crystals [4]. Skyrmion crystals are like Wigner crystals of composite objects, each of which comprises a group of textured spins and acts as a topological defect [5]. Crucially, these crystals exhibit spatial symmetry breaking on top of the internal symmetry breaking. Skyrmion crystals have also been heavily studied in metallic magnets, where they arise due to the Dzyaloshinskii–Moriya interaction, and their detection in such settings was first reported in landmark neutron scattering [6] and electron microscopy experiments [7]. While there has been some indirect evidence for the existence of a quantum Hall skyrmion crystal, via NMR [8,9], heat capacity [10], Raman [11], and

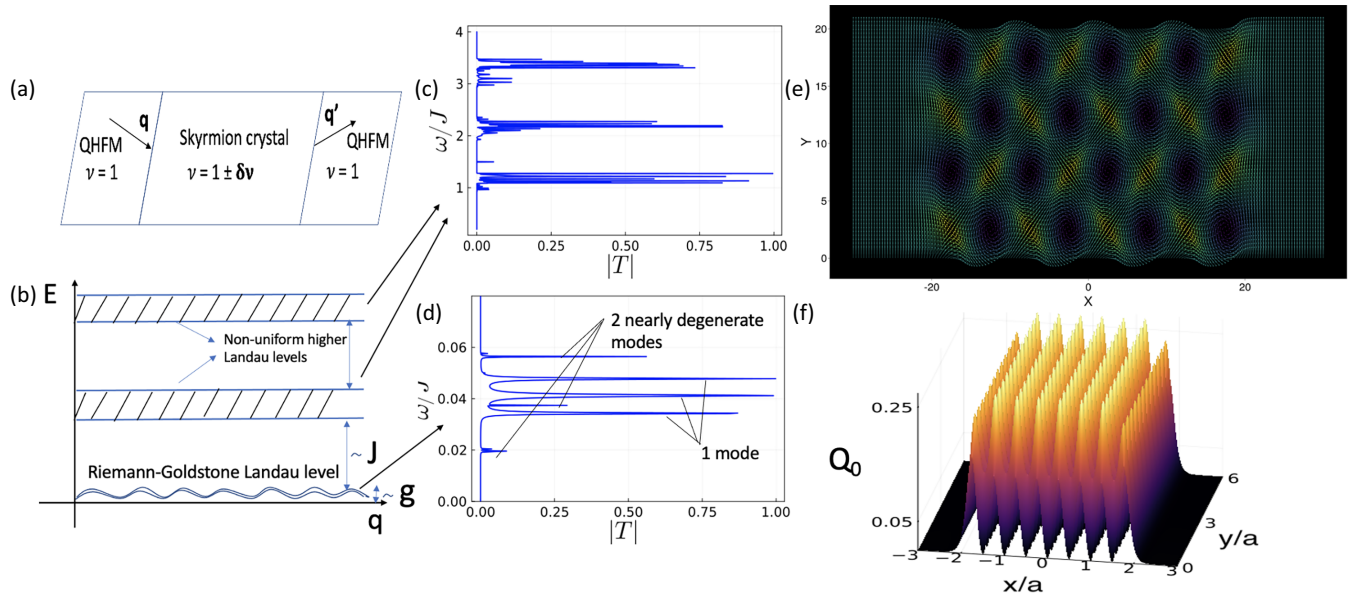*Corresponding author: nilotpal@pks.mpg.de

FIG. 1. Results for the quantum Hall ferromagnet (QHFM)-skyrmion crystal junction. (a) Schematic picture of the scattering problem and the experimental setup—sharp interface drawn only for illustrative purposes. (b) Cartoon description of the spectrum of the skyrmion crystal comprising higher nonuniform Landau levels and the lowest Riemann-Goldstone Landau level. (c) High-energy band-like transmission features due to effective nonuniform Landau levels [generated due to spatially modulated topological charge density profile (with finite nonzero mean) in (f) and not uniform applied external field]. (d) Low-energy transmission features due to presence of Goldstone modes in the Riemann-Goldstone Landau level. Two sets of linearly separated peaks indicating linear dispersion and two distinct velocities of the modes. Small split in peaks with larger spacing (velocity), implies two modes are almost degenerate [see Fig. 9(b) for spectrum]. (e) Spin profile of the junction, from Eq. (6), generated by the truncated holomorphic theta function ansatz in Eq. (7). The tail of every arrow is a lattice site, its direction is the projection on the z-x plane, and the color is the y component. (f) Topological charge density profile for the junction, obtained from Eqs. (5) and (6). Parameters used for (c)–(f) are $g = 0.8$, $J = 1$, $N = 140$, and $N' = 2$

microwave spectroscopy [12] experiments, direct evidence, such as that in an electron microscopy experiment imaging the degree of crystalline order is still missing.

Experimental techniques to detect crystalline ordering and to unveil the excitation spectra of ordered structures have a long history in solid state physics. From Bragg scattering of x-rays to detect crystalline structure of solids, to neutron scattering and ARPES experiments to probe the excitation spectra, with the advent of a new experimental technique, new theoretical explorations are called for.

Recent magnon transport experiments in junctions of quantum Hall states present one such exciting technique [13–17]. While traditional ARPES and neutron scattering experiments are extremely challenging for thin nanomaterials such as graphene, electron transport experiments provide a promising route to probe quantum Hall physics [18,19], especially due to the ability to tune carrier density with voltage in graphene. However, electron transport experiments are largely insensitive to the underlying spin structure of the ground states.

Pioneered in Ref. [13], magnon transport techniques involve a coherent source of magnons, usually a quantum Hall ferromagnet, which are injected into an insulating bulk sandwiched between the leads. These techniques allow us to probe the spin structure of the bulk and have been used to study various ground states expected at different fillings of the zeroth Landau level in monolayer graphene.

Applying these experimental techniques to questions involving the topology-symmetry dichotomy has to face a number of technically and conceptually unavoidable issues.

Concretely, constructing an interface between a skyrmion crystal and a nontopological magnetic state cannot simply be achieved by pasting the two subsystems together along a junction in the way one would, e.g., join a superconductor with a normal metal to observe Andreev reflection. The reason is that the skyrmion is a nonuniform and extended object. An interface will thus minimally need a lateral extent set by the size of the skyrmion itself. Moreover, such a problem is theoretically interesting because skyrmions and their crystals are objects that lie in complex projective spaces [$\mathbb{C}P^{d-1}$ for $SU(d)$ systems], hence the interface problem becomes a nonlinear problem as opposed to the conventional bulk-boundary correspondence in quantum Hall and topological insulators [20,21].

Here, we devise and study a scattering problem, which is motivated by, and amenable to, the above mentioned experimental methods. The set-up consists of a quantum Hall heterojunction [Fig. 1(a)] of a skyrmion crystal sandwiched between two simple quantum Hall ferromagnets, as might be obtained by setting the filling of the outer regions to $\nu = 1$ and doping (or, rather, gating) the central region slightly away from such filling $\nu = 1 \pm \delta\nu$. Such a setup has already been realized in one of the quantum Hall junction experiments [22].

Our central result is that the energy dependence of the magnon transmission amplitude reflects the topology-symmetry dichotomy in exquisite detail, establishing such magnon scattering experiments as an excellent platform to probe this dichotomy. The topology of the skyrmion crystal bequeaths an emergent Landau-level structure to the response; while its lowest Landau level—which we christen

Riemann-Goldstone Landau level—contains the physics of the symmetry breaking itself. Remarkably, from the magnon transmission, one can directly infer the nature of the Goldstone modes, which is characteristic of the skyrmion crystal as well as the effective Landau level structure of the higher levels.

The physics of skyrmions is a very large field of research spanning the fields of high-energy, metallic magnets/spintronics, and quantum Hall physics. Skyrmion crystals, however, appear only in the latter two. In the quantum Hall community there have been previous papers studying the dispersion of infinite skyrmion crystals [23,24]. Similar papers on infinite skyrmion crystals have also been undertaken in metallic magnets, although the microscopic physics there is entirely different and the skyrmions are not electrically charged [25–27]. Moreover, two very influential papers in the spintronics literature studied the interaction of a magnon excitation of a single skyrmion with the skyrmion itself [28,29]. However, these magnon transport techniques present a completely different theoretical and physical problem, shifting from dispersion calculations of infinite skyrmion crystals and studies of skyrmion motion via magnon emission to the interaction of ferromagnetic magnons with a finite skyrmion crystal sandwiched between two ferromagnets. This complex interaction between a boson and an electronic solid of quantum Hall skyrmions serves as a novel framework to explore the rich physics associated with the confluence of topology and symmetry breaking. Moreover, on the macroscopic level, such a theoretical approach is also important for metallic magnets where people have started to explore spin transport through textured domain walls between a ferromagnet and an antiferromagnet [30] and also possibly for electronic transport through periodically modulated regions of artificial gauge fields [31].

A significant fraction of the following account details important technical advancements that we made to fully solve this problem. We focus on advances which are transferable and useful to other contexts and fields in the main text, and discuss some more specific ones in the Appendices. First, we introduce our completely analytical model of a ferromagnet-skyrmion crystal-ferromagnet interface formed from a basis of holomorphic theta functions, as well as a suitably defined energy functional from which we derive our equations of motion. Second, we introduce a method to discretize the topological charge density contributions to the energy functional. Third, we explain our microscopic recursive transfer matrix approach to calculate the full transmission and reflection matrix of the skyrmion crystal scattering problem, even in the presence of evanescent contributions. All these advances can find applications in transport problems between interfaces of such topologically trivial and nontrivial structures and possibly also in transport through regions of spatially varying magnetic field.

For the less technically inclined readers, we supply some simple heuristic models to account for the physical phenomena that we have uncovered. While these do not capture the full complexity of the topology-symmetry dichotomy, they do provide a clear rationale for why the proposed set-up is so well suited for studying this problem, and they yield a transparent and intuitive framework for the interpretation of the full results of our analysis. These heuristic models already provide some predictions which can be tested in future skyrmion crystal junction experiments.

The remainder of our account is structured as follows. Section II provides a short-hand self-contained and largely nontechnical summary of our results. Section III contains some general considerations of the dichotomic structure of the problem which leads to an intuitive picture for the formalism developed in later chapters, and for the interpretation of the results thus obtained: a model of a particle in a heterostructure comprising a modulated magnetic field sandwiched between two zero-field regions provides a simple route to capturing the topological features which are independent of the local symmetry breaking. For the Goldstone sector, we consider a simplified interface between a ferro- and an antiferromagnet on a lattice, which allows us to study the simplest case of a dispersion mismatch problem. We note that it has come as quite a surprise to us that this dichotomy should be so neatly resolvable by this pair of heuristic models.

Section IV is the most technical section of this paper. In Sec. IV A, we introduce our holomorphic theta functions ansatz and our energy functional. In Sec. IV B, we introduce the method to discretize the topological charge density contributions. We end this section with Sec. IV C, where we explain our transfer matrix procedure for the magnon scattering problem. In Sec. V, we present additional results for the quantum Hall ferromagnet-skyrmion crystal-ferromagnet problem which are not discussed in Sec. II, and we highlight similarities with the heuristic models presented in Sec. III. Finally, in Sec. VI, we end by discussing the experimental relevance of our model (Sec. VI A) and further implications of our work (Sec. VI B).

II. OVERVIEW OF RESULTS

Our main result is a calculation of the magnon transmission spectrum across the skyrmion crystal. We find the following characteristic set of signatures in the transmission spectrum which reflect the topology-symmetry dichotomy:

(i) The high-energy transmission spectra comprises sharp peaks in discrete bands of energies, with uniform gaps between the bands as in Fig. 1(c). The sharp peaks within each band arise as a consequence of Fabry-Perot like resonances when the incoming magnon energy coincides with bound states of the scattering problem. Remarkably, these bound states have an emergent Landau-level structure. These levels are emergent because they reflect the spatially modulated topological charge density (which has a finite nonzero mean) of the skyrmion crystal (instead of the applied external constant magnetic field): magnons experience the Berry flux of the spin texture in the central region as an effective magnetic field.

(ii) The lowest-emergent Landau level, which we call the *Riemann-Goldstone Landau level* due to it arising from holomorphic constraints [32] (see Sec. IV A for details), hosts the Goldstone modes associated with the symmetry breaking. The transmission spectrum in this low-energy window exhibits discrete sets of uniformly spaced peaks in a small energy window as in Fig. 1(d).
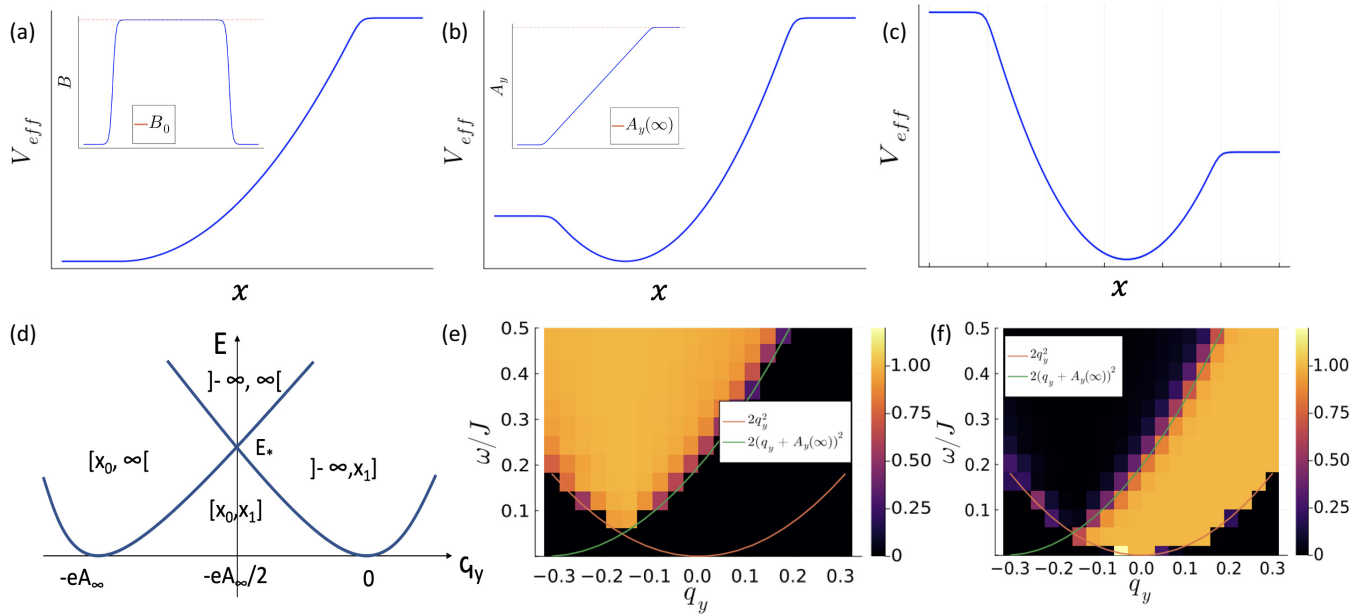
FIG. 2. Semiclassical analysis for heuristic model with constant magnetic field in the central region. All arguments and results in this panel are for the Landau gauge ($A_x = 0$). [(a)–(c)] Qualitatively different effective potentials for different values of transverse momentum, $q_y \geqslant 0$ for (a), $-eA_y(\infty)/2 < q_y < 0$ for (b) and $-eA_y(\infty) < q_y < -eA_y(\infty)/2$ for (c), the $q_y \leqslant -eA_y(\infty)$ case is a reflection of (a). Insets of (a) and (b) show the constant magnetic field profile with smooth decay away from central region and the corresponding vector potential in the Landau gauge respectively. d) Different qualitative regions of scattering in energy-transverse momenta parameter space with the labels in each region indicating the x support of the corresponding semiclassical trajectories—we get two regions of full reflection, $x \in]-\infty, x_1]$ or $x \in [x_0, \infty[$, one region with bound trajectories ($x \in [x_0, x_1]$) and one region with full transmission ($x \in]-\infty, \infty[$). [(e), (f)] Numerically obtained transmission and reflection coefficients respectively for the quantum problem with Hamiltonian in Eq. (1) showing great qualitative agreement with the semiclassical picture in (d). We only consider the case of a particle incident from the left which is why the reflection coefficient in (f) is not fully symmetric as in (d) which considers both left and right incident processes.

Indeed, the effects due to topology and symmetry breaking are delicately intertwined. At high energies, the width of and gaps between these discrete bands of transmission corresponds to the same of the emergent Landau levels, which reflect the topology of the skyrmion crystal (see Fig. 9 and Sec. V). Hence magnon transmission allows one to infer the nature of the high-energy modes of the skyrmion crystal (i.e., modes just above the Goldstone spectrum). On increasing energy the magnon transmission also exhibits a characteristic angular dependence, with certain preferred angles of transmission and a nonmonotonic dependence of transmission on channel number. This dependence reflects the spatial symmetry breaking, i.e., it is a consequence of the crystalline order of the skyrmions. Moreover, the modes in the Riemann-Goldstone Landau level are associated with the SU(2) group manifold acting on the $\mathbb{C}P^1$ local order parameter manifold of the skyrmion crystal. Notably, the uniform spacing within each set of low-energy peaks, indicates the linear dispersion of these Goldstone modes at small momenta. The number of such sets of peaks also directly allows us to infer the presence of three such modes. Hence, not only do these results unambiguously indicate the presence of a skyrmion crystal, they also unveil the nature of its excitation spectrum, both at low and at high energies. Figures 1 and 9 (see below) highlight these points clearly.

Section III A presents a simplified heuristic model, which accounts for the topological—but not the symmetry—aspects of these results. We prepend this discussion, Sec. III A, to

the much more technical analysis by which it was motivated (Sec. IV and Appendix A), where we found that the effective description of the scattering problem bears some resemblance to the problem of a particle scattering off of a region with spatially varying magnetic field: We are led to study a (single) particle scattering off a region with spatially varying magnetic field.

To single out the effect of the variation of the magnetic field, we first consider the problem of a constant magnetic field and map out the transmission and reflection coefficients in energy-momentum space as in Figs. 2(f)–2(h). We find that such a problem is characterized by a critical-energy scale E_* below which there is no transmission, and regions of either full transmission or full reflection with a smooth crossover from one to the other. We also note that there are bound states below E_*, which play an important role on introducing spatial modulations of the magnetic field. Also any nonzero transmission is accompanied by an angular deviation which we calculate as a function of incoming energy and present in Fig. 5(a). These features can be accounted for in a picture of semiclassical cyclotron orbits.

The physics becomes even richer on introducing modulations along the transverse direction, as is present, in a skyrmion crystal. On doing so, we find that there are sharp transmission peaks in the semiclassically forbidden region, i.e., below E_*. Moreover, we find that these peaks have a special structure, they occur in certain energy windows, and these windows have uniform gaps between them as in Fig. 3(a).
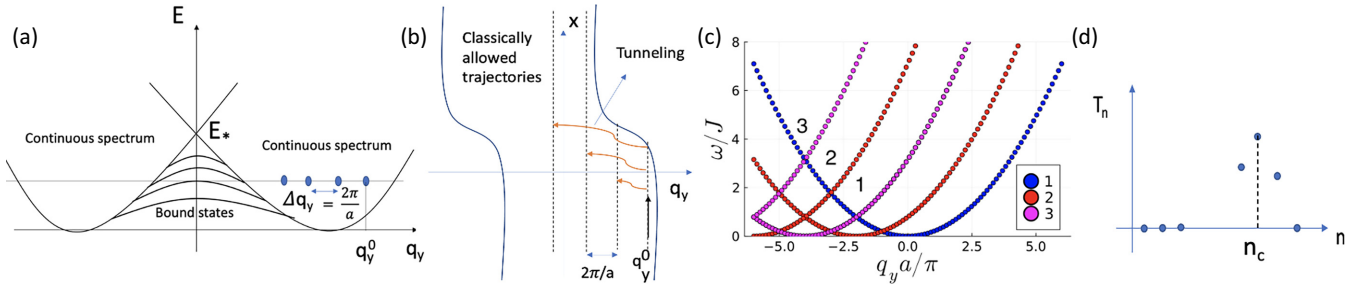
FIG. 3. Qualitative arguments for heuristic model with spatially modulated magnetic field along y axis. (a) Continuous spectrum for scattering and discrete spectrum for bound states. Modulation along transverse directions breaks q_y conservation and periodic modulation implies q_y is conserved modulo $2\pi/a$. Transmission below critical energy E_* is possible if the energy of one of the channels coincides with the bound state. (b) Pictorial description of the possibility of tunneling into other propagating channels due to crystalline order. Each channel has its effective potential profile and regions of allowed transmission as in Fig. 2(c)–2(f). The presence of multiple propagating modes allows transmission for an incoming magnon due to off-diagonal scattering. (c) Number of propagating modes in the $\omega - q_y$ plane in the unfolded zone scheme (for visual reasons). One can transfer this to the first Brillouin zone by standard folding techniques. Each color is for the two curves $2q_{yi}^2$ and $2(q_{yi} + A(\infty))^2$, such that in the region lying above both curves one gets an outgoing propagating mode for the ith channel, where $q_{yi} = q_y^{(0)} + 2\pi(i-1)/a$. For this figure we use $B_0 = 2\pi/a^2$ and $L = 20$. (d) Pictorial description of nonmonotonicity of channel resolved transmission from qualitative arguments presented in Sec. III B and figure (b) in this panel [not real data, see Fig 5(b)].

Such gaps correspond to the Landau level gaps in the spectrum and the energy windows occur due to the dispersion in the Landau levels introduced by the spatial variation. We also find that the heights of most of the transmission peaks are suppressed. These phenomena are in turn accounted for in terms of resonances from bound states, and interference between more than one propagating mode, respectively.

This brings us to our analysis of the full ferromagnet-skyrmion crystal-ferromagnet junction problem, the solution to which requires several technical advancements. We include three such advances in the main text (others are relegated to Appendices) in Sec. IV, which are also applicable to other problems in transport calculations of such junctions between topologically trivial and nontrivial structures. These advancements draw from a wide variety of fields and reflect the richness of this problem.

First, in Sec. IV A, we address the difficult nonlinear problem of constructing an interface between such topologically trivial and nontrivial structures as mentioned in the introduction. We use an analytical ansatz constructed from truncated holomorphic theta functions to model our ferromagnetic-skyrmion crystal-ferromagnetic junction. Using the theta functions in Eq. (7) as basis functions, we can generate a textured skyrmion crystal with two skyrmions per unit cell in the central region with similarly aligned ferromagnets on the two sides as shown in Fig. 1(e). On calculating the topological charge density from these truncated theta functions, using Eq. (5), as in Fig. 1(f), we see that we get periodic modulations of the topological charge density in the central region and a smooth decay to zero away from it. The region across which we get a smooth decay defines the interface. Similar holomorphic constructions can be used for other topological structures and can also be extended for fractional or entanglement skyrmion crystals [33].

Using these theta functions, we reverse engineer an energy functional with short range interactions and with the spin configuration in Fig. 1(e) as the minima in the continuum limit. We calculate the equations of motion for the excitations of this using techniques from linear spin-wave theory in Appendix. It

is the form of the variation in the energy functional, given in Eq. (11), which resembles the free particle problem discussed in the previous paragraphs.

Any microscopic numerical calculation of the transport properties of such junctions requires real-space discretization of the continuum energy functional in Eq. (11). Discretizing the exchange term is a standard exercise in finite difference methods; however, discretizing the change in topological charge density is highly nontrivial task. In Sec. IV B we introduce a geometrical method to do this discretization in a completely analytical way. Our approach relies on the short-range nature of our interaction, which allows us to express the topological charge density in terms of the solid angle subtended by the four geodesics connecting the four spin vectors of a real-space plaquette on the Bloch sphere. Our final result in Eq. (22) expresses the discretized form of the second term in Eq. (11) as a tight-binding model with up to second-nearest-neighbor hopping.

To calculate the full magnon transmission matrix, we use a recursive transfer matrix approach explained in Sec. IV C. First, we discretize the energy functional in real space using standard finite difference methods for the exchange term and the topological charge discretization procedure given in Sec. IV B. The usual recursive columnwise procedure involves multiplying the transfer matrix at every column and forming a product matrix which relates the left and right ends of the problem. However, such an approach runs into problems in the presence of evanescent contributions, which cause a numerical instability in obtaining the final product matrix. We resolve this instability by adapting a method introduced by Pendry for similar problems in optics [34]. This method allows us to obtain the full transmission matrix for the magnon and hence gives us access to channel resolved transmission coefficients.

Section V provides additional numerical results for the full problem of the skyrmion crystal junction, as summarised at the very beginning of this section, and using the technical advancements made in Secs. IV A–IV C. We also obtain the spectra of the high-energy modes and show how the transmission energy windows correspond exactly to the energies

of these emergent Landau levels. Further, we comment on how the heuristic model of a particle scattering in a region of spatially varying magnetic field qualitatively captures the behavior in this energy regime. However, the transmission features at low energies cannot be understood from that heuristic framework, since that framework has no Goldstone modes. We obtain the dispersion of these Goldstone modes, as in Fig. 9(b) and show how the transmission varies on varying their dispersion. On increasing dispersion, the discrete low-energy peaks in transmission shift in position and their intensity increases as in Fig. 9(a). The transmission spectra in this regime has qualitative similarities with the heuristic model for the antiferromagnet sandwich, which we introduce in Sec. III D and hence one can borrow our intuitive understanding from that analysis.

As a significant motivation of our paper were the experimental advances described in the introduction, in Sec. VI A we present arguments for how our theoretical predictions can be experimentally tested in a $\nu = 1 : 1 \pm \delta\nu : 1$ quantum Hall junction on monolayer graphene. There are elements of our model that might not be completely realistic such as absence of anisotropies, delta function interaction potential, and a smooth interface. In Sec. VI A, we comment on how the presence of realistic anisotropies might change some low-energy signatures by gapping out a subset of the Goldstone modes but some signatures of the remaining gapless modes shall remain. We comment on how to realize short-range interaction using metallic gates and finally we comment on situations where the interface is sharper than in our model. We finally close with an outlook in Sec. VI B.

III. HEURISTIC MAGNON SCATTERING

In this section we provide details of two heuristic models as mentioned in the earlier sections. In the first three subsections we introduce and study a particle scattering off a region with (i) a constant and then (ii) a spatially modulated magnetic field. The spatial profile of the magnetic field mimics that of the topological charge density in the skyrmion crystal junction. This heuristic model turns out to be useful since (as shown in the next section and in Appendix A) it turns out to qualitatively describe (primarily the) topological aspects of the skyrmion crystal problem. In the last subsection we introduce a simple model to discuss the coupling between qualitatively different kinds of Goldstone modes, namely a ferromagnet-antiferromagnet-ferromagnet junction. Both these models allow us a simpler and intuitive understanding of complementary parts of the difficult and technically involved problem fleshed out in Secs. IV and V.

A. Particle scattering off a region of constant magnetic field

To isolate the effect of spatial modulations in the magnetic field we first consider a constant magnetic field profile in the central region, which exponentially decays to zero across the interface as shown in the inset of Fig. 2(a). Such a system, in the Landau gauge ($A_x = 0$, $B(x) = \partial_x A_y(x)$), has the Hamiltonian

$$H = \frac{1}{2m}\left[q_x^2 + (q_y + eA_y(x))^2\right]. \tag{1}$$

We consider the following magnetic field profile $B_c = B_0/2(\tanh(x - L/2) - \tanh(x + L/2))$ as in Fig. 2(a), where B_0 is the value of the magnetic field in the central region of length L. Throughout this discussion, we use a gauge in which $A_y(-\infty) = 0$ and $A_y(x)$ is a positive and increasing function of x with a saturation value $A_y(\infty)$ as shown in the inset of Fig. 2(b).

Since we have translational invariance along y, we have two degrees of freedom and two conserved quantities, the total energy E and the transverse momentum q_y. Hence, we have an integrable system.

Let us understand the semiclassical trajectories for such a system. Since q_y is conserved we get a collection of one dimensional models with an effective potential $V_{\text{eff}}(x, q_y) = (q_y + eA_y(x))^2/(2m)$.

As a function of x, qualitatively, we have three different types of effective potential depending on q_y. (i) If $q_y \gtrsim 0$, V_{eff} is monotonically increasing with $V_{\min} = q_y^2/(2m)$ and $V_{\max} = (q_y + aA_y(\infty))^2/(2m)$ as in Fig. 2(a). For $-eA_y(\infty) < q_y < 0$, by contrast, $q_y + eA_y(\infty)$ changes sign at x_* and we get two types of potential curves, (ii) for $-eA_y(\infty)/2 < q_y < 0$, as in Fig. 2(b), and (iii) for $-eA_y(\infty) < q_y < -eA_y(\infty)/2$, V_{eff} is as in Fig. 2(c). Finally for $q_y \lesssim -eA_y(\infty)$, V_{eff} is monotonically decreasing and looks like the reflection of Fig. 2(a).

For each region, the support in x of the corresponding trajectory depends on the incoming particle energy E. If $E < V_{\min}$, no scattering states exist, if $V_{\min} < E < V_{\max}$, the classical trajectories are purely reflected, i.e., the radius of the cyclotron orbits is less than the length of the central region.

Already at this simplistic level, we can see that if the particle is transmitted, i.e., the radius of the cyclotron orbit is larger than the length of central region, then particle will exit the central region with a velocity different from its incoming velocity and its direction will be deflected. One can calculate the angle of deflection easily: say the incoming velocity is $\boldsymbol{q}$, the outgoing velocity on the right end will be $\boldsymbol{q} + \boldsymbol{A}_\infty$. In the Landau gauge, $A_x = 0$, therefore, the outgoing velocity will be $\boldsymbol{q} + A_y(\infty)\hat{\boldsymbol{y}}$. Hence, the angle of deviation is given by $\cos^{-1}[\boldsymbol{q} \cdot (\boldsymbol{q} + A_y(\infty)\hat{\boldsymbol{y}})/(|\boldsymbol{q}||\boldsymbol{q} + A_y(\infty)\hat{\boldsymbol{y}}|)]$. This effect resembles that of the magnon Hall effect, studied in magnon scattering off of single skyrmions in metallic magnets [28,29].

The most interesting region is the low-energy regime $0 < E < E_*$, where $E_* = (eA_y(\infty)/2)^2/(2m)$. In this case, the semiclassical solutions (and also the corresponding eigenstates for the quantum version) depend on q_y, but there is no extended state going from $x = -\infty$ to $x = \infty$: the transmission coefficient across the central region exactly vanishes for $E < E_*$. However, in a window in the $E - q_y$ parameter space, there exist classically bound trajectories (closed cyclotron orbits in the central region) for $E < E_*$. In the quantum problem, the bound states of the classical picture correspond to Landau levels, which will play an important role once the magnetic field in the central region is modulated, as is the case in the actual skyrmion crystal junction.

To confirm this above picture, we calculate the reflection and transmission probabilities starting from our Hamiltonian in Eq. (1). We see that our numerical results in Figs. 2(e)–2(f) agree very well with the semiclassical analysis in presented
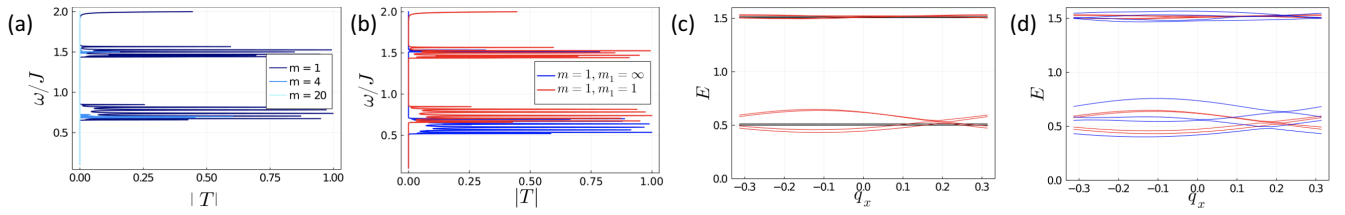
FIG. 4. Results for heuristic model with spatially varying magnetic field. (a) Transmission spectra for a particle scattering off a region with periodic modulation, see main text, of magnetic field along y axis, where m is the parameter that controls the amplitude of modulation, $B = B_c(\sin(4\pi y/a)/m + 1)$, and B_c is the magnetic field used in the last subsection. Small m implies large modulation and vice versa. The case with $m = 1$ resembles the same amplitude of modulation along y axis as in the topological charge density profile in Fig. 1(f). (b) Transmission spectra for the case of a magnetic field modulated along x and y axes, where m_1 has the same properties as m described, but for the x axis in (a). The case with $m = 1, m_1 = 1$ resembles the same modulation along both axes as in the topological charge density profile in Fig. 1(f). (c) Effect of modulation along y on Landau levels, adds bandwidth. (d) Effect of modulation along x on Landau levels, reduces gap. Black lines in (c) and (d) are for the unmodulated magnetic field case, red for the case with large modulations only along y axis, and blue for the case with large modulations along both x and y axis.

above and summarized in Fig. 2(d). There exists a minimum energy E_* below which there is no transmission, the threshold energy for transmission depends on the transverse momentum and as expected for the quantum problem there is a smooth evolution from full reflection to full transmission on increasing energy at fixed q_y. Also, there is an angular deviation in the region of full transmission as in Fig. 5(a).

B. Effect of periodic modulation along y axis

Our analysis of semiclassical trajectories showed that a constant magnetic field in the central region implies that there is no transmission below a certain threshold E_*, yielding distinct regions of full transmission and full reflection in $E - q_y$ parameter space. Quantum mechanically, regions where the x support of classical trajectories is infinite have a continuous spectrum whereas the bound-state region, which has only a finite support $[x_0, x_1]$, has a discrete Landau level spectrum. The bound states have slightly bent dispersion because the local potential wells around x_* become very shallow as $x_* \to \pm\infty$, see Fig. 3(a). In this and the following subsection we address the effects of periodic modulation of B about its mean B_0 in the central region. Again, we examine the heuristic model given by Eq. (1), but now, first with a periodic modulation of B along the transverse (y) direction.

A periodic modulation of period a in the y direction breaks q_y conservation and hence generates matrix elements between states with q_y values differing by integer multiples of $2\pi/a$. This mechanism generates a tunneling amplitude to an order N_p in perturbation theory given approximately by $2\pi N_p/a \approx eA_y(\infty) = B_0 L/\phi_0$, so $N_p \approx B_0 aL/(2\pi\phi_0)$, where B_0 is the average magnetic field in the central region and ϕ_0 is the flux quantum. If E lies in the gap of the bound-state spectrum, since $N_p \sim L$, the corresponding transmission amplitude will be exponentially small in L. However, importantly there will be some resonances for $(q_y^{(0)}, E)$ values such that E coincides with a bound state (i.e., a state of the Landau level) with energy at $q_y^{(n)} = q_y^{(0)} + 2n\pi/a, n \in \mathbb{Z}$. Such resonances permit transmission at energies below the threshold E_*.

Once q_y conservation is broken, the scattering problem becomes a multichannel problem, where the number of channels depends on the discretization procedure. The presence of multiple channels makes the problem very rich and we devise a transfer matrix procedure, which calculates the full transmission matrix, which allows us to obtain the channel resolved transmission. Say, we consider an N channel problem based on the discretization of the $a \times a$ unit cell into $a/N \times a/N$ grids. Out of the N possible values of q_y, some values will represent propagating channels, $\text{Im}(q_x = 0)$, whereas, for relevant energy scales and N values, most channels will be evanescent, $\text{Im}(q_x \neq 0)$.

To extend our heuristic picture to this multichannel problem, one can examine the effective potentials, as in the constant B case, for each of the q_y channels. For energies $E_* < E < V_{\max}(q_y^{(0)})$, in the constant magnetic field case there is no transmission and hence full reflection, $|T| = 0, |R| = 1$. However, for the modulated case, there exist channels such that $E_* < V_{\max}(q_y^{(n)}) < E$, hence there will be transmission through these channels. Moreover, there will be a nonmonotonic dependence of the transmission amplitudes on the channel number, with maximal transmission for $n = n_c$, as depicted pictorially in Fig. 3(d). Further, the channel number of the maximally transmitted channel will increase on increasing energy.

Following from this qualitative picture based on the multichannel scattering analysis, we proceed to implement the above problem numerically using our transfer matrix approach described in Sec. IV C. In the Landau gauge the right end of the junction had a finite nonzero vector potential $A_y(\infty)$. However, in the actual experiment there is no such vector potential in the ferromagnetic end, hence to enable direct comparison we also implement a gauge fixing procedure using a string of Aharanov-Bohm fluxes, aided by our problem being discretized on a lattice, to ensure that the vector potential vanishes on the right end (see Appendix D for details).

We choose a magnetic field profile with sinusoidal modulations along the y axis with period $a/2$, $B = B_c(\sin(4\pi y/a)/m + 1)$, where B_c is the magnetic field used in the last subsection. m controls the amplitude of transverse modulation, with large m implying small modulations and vice versa. From Fig. 4(a) we see that for small or negligible variations along the y axis, there is no transmission for the plotted energy range, since for these energies and for this value of B_0, the incoming energy is lower than the

critical energy required for transmission. For $B_0 = 8\pi/a^2$, $a = 10$, and $L = 4a$, we get $E_* = (16\pi/a)^2/2 \gg 2$, in units of $e = m = J = 1$ (see Sec. V A for reasoning for such values of parameters). However, for large modulations, and more importantly for modulations, which mimic the topological charge modulations (in the y direction) of the SU(2) skyrmion crystal [see Fig. 1(b)], we see a dramatic change in behavior, characterized by the appearance of resonant peaks of finite transmission. Moreover, these peaks appear in discrete regions of energy centered around energies corresponding to the different Landau levels of the constant magnetic field problem. This confirms the qualitative picture we developed in the last section, in which finite transmission below the threshold energy takes place when the incoming particle energy coincides with the bound-state energy for certain channels. The transmission windows also allow one to infer the width of such effective Landau level bound states.

Besides the resonant transmission features below the critical energy, we also verify the nonmonotonic channel dependence of transmission for energies above the critical energy by plotting the channel-resolved transmission coefficients in Fig. 5(b). Similar nonmonotonic transmission and angular dependence will be observed in skyrmion crystal junctions. In Fig. 5(b), we see that in different energy windows different channels dominate transmission, and there is a nonmonotonic channel number dependence. Moreover, from our intuitive picture of off diagonal scattering one can predict exactly which channel dominates transmission in the different energy windows. However, the details for which channel dominates depend on the length of the skyrmion crystal region and we leave that analysis for future more experimentally specific work.

One surprising result that is not captured by our earlier qualitative analysis is the varying height of the transmission peaks corresponding to the different Landau levels. Some peaks in the energy range of the higher Landau levels appear to be suppressed. Such a suppression in peak height can be understood as a consequence of interference between multiple propagating channels in the central region. Appendix E presents a detailed technical discussion of the effect of multi-mode interference on the peak heights.

C. Effect of periodic modulation along x axis

From the above two subsections, we see that a periodic modulation of the magnetic field along y axis induces resonant peaks of finite transmission at energies corresponding to low-lying Landau level energies of the constant magnetic field problem. Hence, due to the gap between Landau levels, we also see a gap between regions of finite transmission as in Fig. 4(a). We now complete the analogy of our heuristic model with the skyrmion crystal by introducing its final ingredient, the modulation of the magnetic field along the x axis on top of the modulations along y. We use a similar sinusoidal variation dependent on parameter m_1 (large m_1 corresponds to small variation and vice versa).

Variations of the magnetic field along the x axis broaden the Landau levels and hence the gap between the regions of finite transmission decreases. This is shown in Figs. 4(b) and 4(d), obtained from our numerics, where we see that for
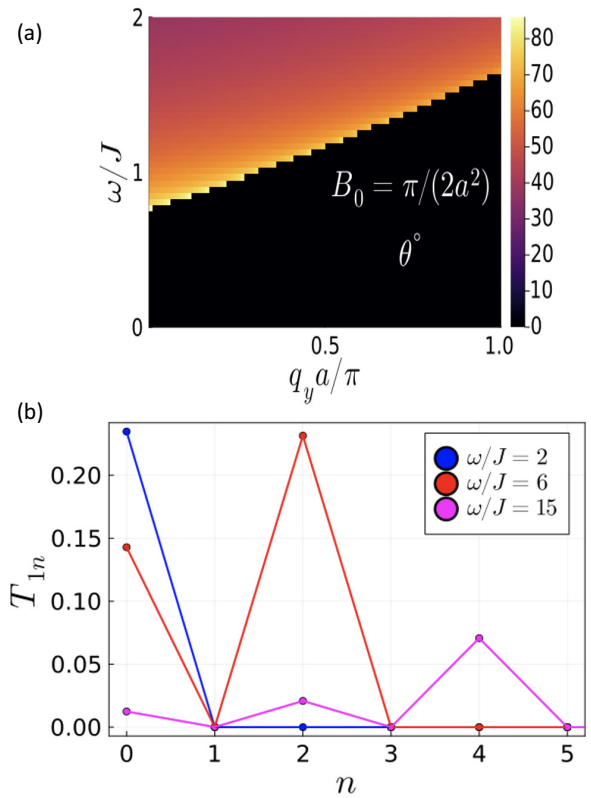

FIG. 5. Channel dependence and angular deviation of transmission for the heuristic model in Secs. III A–III C. (a) Angular deviation of particle scattering off a constant magnetic field region, similar to magnon scattering off a single skyrmion. (b) Channel dependence of transmission coefficient for spatially modulated magnetic field ($B_0 = 8\pi/a^2$, $L = 20$, $m = 1$, $m_1 = 1$, $q_y^{(0)} = 0$). Certain channels dominate in certain energy regions, and there is a nonmonotonic dependence of transmission coefficient on outgoing channel number n, where $q_y^{(n)} = q_y^{(0)} + 2(n-1)\pi/a$. For low energies, below E_*, only one propagating channel is present $q_y^{(0)}$. On increasing energy the number of propagating channels increases as shown in Fig. 3(c), and the particle can scatter into these channels (the transmission matrix has nonzero off diagonal elements). This agrees with the qualitative picture of tunneling into other propagating channels, as presented in Sec. III and Fig. 3(b).

a modulation amplitude that mimics the topological charge density modulation along the x axis of the skyrmion crystal (i.e., for $m_1 = 1$), the gap is reduced. Hence a modulation of the magnetic field along the x axis increases the energy range of finite transmission due to Landau-level broadening.

D. Ferromagnet-antiferromagnet-ferromagnet junction—Effect of dispersion mismatch

Our heuristic model in the previous three subsections did not involve the physics of Goldstone modes arising from symmetry-breaking of the skyrmion crystal. To highlight the issues involved in the transmission properties of a magnon through structures with not only different dispersion relations but also a different number of collective modes, we consider a very simple model of an antiferromagnet sandwiched between two ferromagnets. The dispersion relation of a
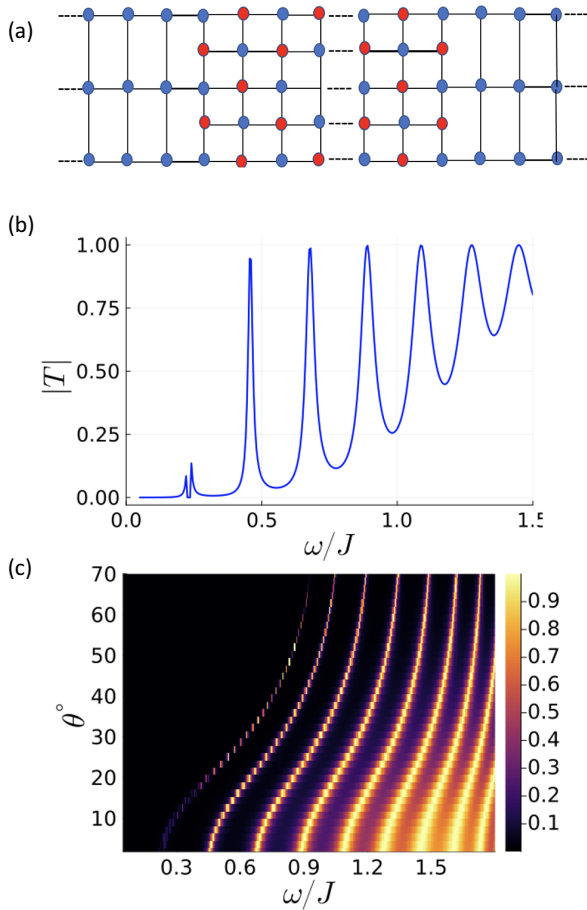
FIG. 6. Results for the ferromagnet-antiferromagnet-ferromagnet quantum Hall junction heuristic model- parameters used $J_F = 1, J_{AF} = 1, L_I = 18a_x$, where a_x is the lattice spacing along x. (a) Lattice structure of the heuristic model with the y spacing for the ferromagnet twice that of the x spacing. Such a simplification is made to simplify the sublattice matching across the interface. (b) Fabry-Perot resonance peaks at normal incidence ($q_y = 0$, $\theta = 0$) in the total transmission. (c) Transmission as a function of angle of incidence and energy of incident magnon. At fixed angle of incidence, there is a critical energy for transmission following which there is a set of equally spaced peaks in the low-energy regime, reflecting the linear nature of the antiferromagnetic Goldstone modes. The cutoff energy at $\theta = 0$, is a finite size effect, as we increase the length of the middle region, this value will go closer to zero.

ferromagnetic magnon is $\sim J_F k^2$ whereas that of an antiferromagnetic magnon is $\sim J_{AF} k$. Moreover, the antiferromagnet has two branches of Goldstone modes as opposed to the single one in the ferromagnet.

We construct a very simple sandwich structure, which makes our calculations entirely analytically tractable. We consider an antiferromagnet with half the lattice spacing in the y direction of the ferromagnet, so that only the A sublattice sites in the antiferromagnet are connected to the ferromagnet [as shown in Fig. 6(a)]. We then solve the scattering problem for a magnon injected from the ferromagnetic region on the left with the following form of the complex wavefunction in the ferromagnetic regions, $x \geqslant L_I$, which describes the spin

deviation perpendicular to the equilibrium magnetization

$$\delta n_F(x, y) = \begin{cases} Ae^{ik_x x + ik_y y} + Be^{-ik_x x + ik_y y}; & x \leqslant -L \\ Ge^{ik_x x + ik_y y} \end{cases} \quad (2)$$

whereas in the antiferromagnet, $|x| \leqslant L_I$, due to the presence of two modes, the same can be written as

$$\delta n_{AF}(x, y) = Ce^{ik_{1x} x + ik_y y} + De^{-ik_{1x} x + ik_y y}$$
$$+ Ee^{ik_{2x} x + ik_y y} + Fe^{-ik_{2x} x + ik_y y}, \quad (3)$$

where $x = -L_I$ and $x = L_I$ are the positions of the interfaces, k_x and k_y are the incoming parallel and transverse momenta of the magnon, $k_{(1/2)x}$ are the parallel momenta of the two modes in the antiferromagnetic region, and the capital letters denote the amplitudes of the various left- and right-moving waves. The transverse momentum k_y is conserved and is hence a good quantum number for the scattering process. We then match the wavefunction across the two interfaces as in standard scattering problems to get the transmission and reflection amplitudes. The total transmission coefficient for the outgoing magnon in the right ferromagnetic lead is given by $|T| = |G|^2/|A|^2$ and the total reflection coefficient for the reflected magnon in the left ferromagnetic lead is given by $|R| = |B|^2/|A|^2$.

This very simple model already exhibits various qualitative features, which carry over to the case of the skyrmion crystal we are interested in. First, in much of the parameter space in Fig. 6(c), transmission is suppressed. Second, at a fixed angle of incidence of the incoming magnon, there is a cutoff energy due to the dispersion mismatch below which the entire wave is reflected for all angles. For low energies, this cutoff energy can be rephrased as a cutoff angle above which one gets no transmission.

Beyond the cutoff energy we get a series of peaks in the transmission amplitude, which broaden on increasing energy. These peaks are essentially Fabry-Perot interference peaks due to multiple reflections within the sandwiched structure. One can also verify that the width of these peaks depends on the length of the sandwiched structure, as expected for Fabry-Perot peaks. Also, at a fixed transverse momentum, or incident angle, the low-energy peaks are equidistant. This reflects the characteristic linear dispersion of the Goldstone modes in the antiferromagnet. As we increase energy, the equidistant nature disappears as the dispersion relation ceases to be linear.

In closing, we note that despite its simplicity, this model reproduces similar qualitative features (the interference pattern and critical angle curve) as the $\nu = 1 : 0 : 1$ quantum Hall junction, where the sandwiched structure hosts a canted antiferromagnetic ground state, which was studied analytically [35] and numerically [36] using Hartree-Fock methods.

IV. SETUP AND SOLUTION OF THE SCATTERING PROBLEM FOR THE SKYRMION CRYSTAL JUNCTION

In this section, we present in turn the central technical aspects of our solution of the full scattering problem of magnons off the symmetry-breaking skyrmion crystal.

A. Basis for smoothly decaying topological charge—Truncated theta functions

A quantum Hall junction with an SU(2) skyrmion crystal sandwiched between two ferromagnets appears as the result of an externally imposed spatial variation of the electrostatic potential seen by electrons in the 2D layer. Neglecting all anisotropic couplings in spin space, the total energy of the quantum Hall ferromagnet is given by the following functional [3,37]:

$$E(\mathbf{n}) = J \int [(\partial_x \mathbf{n})^2 + (\partial_y \mathbf{n})^2] d^2 \mathbf{r}$$
$$+ \int (Q(\mathbf{r}) - Q_0(\mathbf{r})) V(\mathbf{r} - \mathbf{r}') (Q(\mathbf{r}')$$
$$- Q_0(\mathbf{r}')) d^2 \mathbf{r} \, d^2 \mathbf{r}', \qquad (4)$$

where the unit vector $n(\mathbf{r})$ denotes the local spin orientation, $V(\mathbf{r} - \mathbf{r}')$ is the two-body (possibly screened) Coulomb potential, $Q(\mathbf{r})$ is the local topological charge density (which is proportional to the local charge density), and J is a local exchange energy also due to Coulomb interactions. In the case of unscreened Coulomb interactions, $J = e^2/(32\sqrt{2\pi}\epsilon l_B)$ in Gaussian units, l_B being the magnetic length, and ϵ is the dielectric constant. The presence of the imposed external potential is taken into account through the background charge $Q_0(\mathbf{r})$, which we assume to be significant in an infinite (along x axis) slab of finite width parallel to the y axis. The topological charge density is given by

$$Q(\mathbf{r}) = \frac{1}{4\pi} \mathbf{n} \cdot (\partial_x \mathbf{n} \times \partial_y \mathbf{n}). \qquad (5)$$

Minimizing the above energy functional in the presence of the prescribed background charge Q_0 is a difficult and highly nonlinear problem. Casting this in an analytical form is yet more challenging. Furthermore, in a given experimental setting, determining precisely the actual $Q_0(\mathbf{r})$ is also not at all straightforward.

For these reasons, and because our goal is to investigate magnon dynamics, we start by constructing a plausible Ansatz for the spin configuration $n(\mathbf{r})$, which interpolates between a region of finite and spatially modulating topological charge for the skyrmion crystal in the middle to a zero-charge region to the two ferromagnetic ends.

Skyrmion crystals with periodic boundary conditions were previously studied using a basis of theta functions, which are used to construct holomorphic spinors with values in the complex projective space $\mathbb{C}P^{d-1}$ [24]. Such theta functions were first introduced by Haldane and Rezayi in the quantum Hall setting for constructing Laughlin-Jastrow wavefunctions under periodic boundary conditions [38].

In the present paper, we focus on SU(2) spins described by a two-component spinor field $|\psi(\mathbf{r})\rangle$. The relation between this local spinor and the spin orientation vector $n(\mathbf{r})$ is given by

$$\mathbf{n}(\mathbf{r}) = \frac{\langle \psi(\mathbf{r}) | \boldsymbol{\sigma} | \psi(\mathbf{r}) \rangle}{\langle \psi(\mathbf{r}) | \psi(\mathbf{r}) \rangle}, \qquad (6)$$

where σ^x, σ^y, and σ^z are the Pauli matrices. Because multiplying the local spinor by an arbitrary phase factor does not change the physically observable spin orientation, $|\psi(\mathbf{r})\rangle$ can

be considered as an element of the complex projective space $\mathbb{C}P^1$, which is the same manifold as the S^2 sphere, which is the $d = 2$ case, although the present construction easily generalizes to arbitrary integer values of d.

In our model for the skyrmion crystal junction, we have periodic boundary conditions in the y direction and open boundary conditions in the x direction. To model the finite-x support of the crystal we sharply truncate the theta functions whose sum, instead of taken to infinity as is done for periodic skyrmion crystals, is cutoff to the range of integers between $-N' - p/d$ and $N' - p/d$, where $N' \in \mathbb{Z}^+$. For d skyrmions in a $b \times a$ unit cell, the relevant truncated theta functions are given by

$$\theta_p^{(N')}(z) = \sum_{n=-N'-p/d}^{N'-p/d} e^{-\pi bd \frac{d}{a}(n+p/d)^2 + 2\pi \frac{d}{a}(n+p/d)z}, \qquad (7)$$

where $z = x + iy$. The zeros of the theta function indicate the position of skyrmion cores, and p runs from 0 to $d - 1$ in agreement with the Riemann-Roch theorem [32]. Usual θ functions (corresponding to N' infinite) are characterized by the following relations:

$$\theta_p(z + ia) = \theta_p(z), \qquad (8)$$

$$\theta_p(z + b) = e^{(\pi b + 2\pi)\frac{d}{a}z}\theta_p. \qquad (9)$$

The different θ_p functions are related by the following translation operators:

$$\theta_{p+1}(z) = e^{-\frac{\pi b}{da} + \frac{2\pi}{a}z}\theta_p(z - b/d). \qquad (10)$$

At finite N', translational symmetry along y is preserved, but not along the x axis. Using these truncated θ functions we construct the holomorphic spinor defined by $|\psi(\mathbf{r})\rangle_0 = (\theta_0^{(N')}(z), \theta_1^{(N')}(z))^T$. From Eq. (6), this defines the reference spin configuration $\mathbf{n}_0(\mathbf{r})$.

The minimal spin configuration and corresponding topological charge density profile for the ferromagnet-skyrmion crystal-ferromagnet junction generated by these theta functions, and using Eq. (5), is shown in Figs. 1(e) and 1(f). We see that the topological charge density is nonzero and spatially modulated along both x and y axes, with period $a/2$ in the central region outside which it decays smoothly to zero. A sharp cutoff in the theta functions thus leads to a smooth decay of the topological charge density. This allows us to define the notion of an interface for the junction as the region across which the topological charge density goes to zero. Furthermore, one can tune the length of the skyrmion crystal formed the by these truncated theta functions by varying the cutoff N'.

In order to investigate magnon dynamics, we need to specify the energy functional, which is minimized by the reference spin configuration $\mathbf{n}_0(\mathbf{r})$. Because holomorphic spinors always generate local minima for the local exchange term, it is sufficient to set the background charge $Q_0(\mathbf{r})$ in Eq. (4) equal to the topological charge density of the reference configuration $\mathbf{n}_0(\mathbf{r})$. In our calculations, we have replaced the nonlocal Coulomb interaction in the second term of Eq. (4) by a local "Coulomb interaction" (delta function in real space) to simplify the calculations and make our problem partly analytically tractable. Therefore, the corresponding functional

becomes

$$E(\mathbf{n}) = J \int [(\partial_x \mathbf{n})^2 + (\partial_y \mathbf{n})^2] d^2 \mathbf{r}$$
$$+ g \int (Q(\mathbf{r}) - Q_0(\mathbf{r}))^2 d^2 \mathbf{r}. \qquad (11)$$

Moreover, such a delta function interaction term can be realized in quantum Hall junction experiments in graphene with metallic gates (see discussion in Sec. VI).

Without any interaction term, i.e., $g = 0$, all holomorphic functions give the same exchange energy. This renders the magnons nondispersive and localized, which motivated us to call the collection of the corresponding set of states the *Riemann-Goldstone Landau level*. This also shows that we need $g > 0$ to get a finite dispersion of these Goldstone modes. However, the phonon mode in our setup shall remain gapped since the spatial modulations of the topological charge density $Q_0(\mathbf{r})$ in our junction energy functional explicitly break translational symmetry. We comment more on the implications of such a gapped magnetophonon in Sec. VI A where we discuss various other experimental considerations.

Equation (11) is the starting point from which we derive equations of motion using spin-wave theory techniques. First we introduce small deviations $\delta n(r, t)$ about the reference configuration $n_0(r)$. We then express this deviation in terms of local coordinates $\chi_1(r)$ and $\chi_2(r)$ and local orthonormal frames $e_1(r)$ and $e_2(r)$. Now on doing the usual spin-wave theory calculations and imposing the holomorphic constraint arising from minimizing the exchange energy at fixed topological charge (see Appendices A–C for details of the calculation), one can express the second-order variation in the above energy functional due to this deviation as

$$\delta E^{(2)} = g \int \delta Q(\mathbf{r})^2 + J \int \left[|i\partial_x \chi + A_x \chi|^2 + |i\partial_y \chi + A_y \chi|^2 \right.$$
$$\left. - (c_{1x}^2 + c_{2x}^2)|\chi|^2 \right] dx dy, \qquad (12)$$

where $A_{x/y} = \hat{e}_1 \cdot \partial_{x/y} \hat{e}_2$, $c_{1x/y} = \hat{e}_1 \cdot \partial_{x/y} n_0$, and $c_{2x/y} = \hat{e}_2 \cdot \partial_{x/y} n_0$. We find that the second-order variation of the exchange term can be interpreted as the energy of a quantum particle described by a wavefunction $\chi(\mathbf{r}) = \chi_1(\mathbf{r}) + i\chi_2(\mathbf{r})$, $\bar{\chi}(\mathbf{r}) = \chi_1(\mathbf{r}) - i\chi_2(\mathbf{r})$ and subject to a vector potential $\mathbf{A}$, an effective magnetic field $B = 4\pi Q_0$, and a scalar potential $c_{1x}^2 + c_{2x}^2$ (see Appendices B and C for more details on the effect of the holomorphic constraint and gauge invariance of the energy functional). The local frames $e_1(r)$ and $e_2(r)$ are two vectors orthogonal to each other and to $n_0(r)$. In the ferromagnet, if one considers the spin to be polarized along z axis, these frames are just the x and y axes; however, in the skyrmion crystal region, these vectors depend on position. It is in this region that the vector potentials gain a nonzero value, since the dot product defining them is no longer zero as in the ferromagnet.

The physical origin of this effective magnetic field comes from the Berry phase picked up by the magnon when traversing through the skyrmion crystal. Hence, while true that magnons are neutral objects, the interesting physics arises from the topological charge density acting as an effective magnetic field, under which the magnons appear charged. Moreover, in a ferromagnetic region the magnon has a dis-
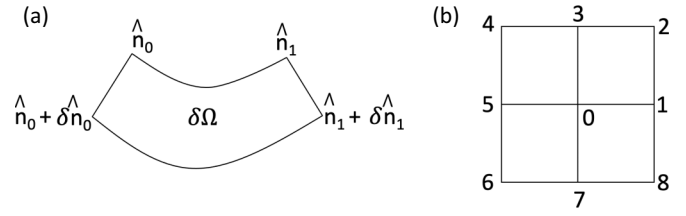

FIG. 7. (a) Change in solid angle between two geodesics on the sphere. (b) Plaquette-wise discretization of topological charge. Tight-binding model includes contributions of nearest and second-nearest neighbors (shown here for site 0).

persion $\omega \sim k^2$ similar to that of a massive particle in nonrelativistic quantum mechanics. These points justify the use of our heuristic model in Secs. III A–III C.

The resulting linearized Landau-Lifshitz equations of motion for such a system can be expressed as a time-dependent Schrödinger equation

$$\alpha \frac{\partial \chi}{\partial t} = 2i \frac{\delta E^{(2)}}{\delta \bar{\chi}}, \qquad (13)$$

where $\alpha = \hbar/(4\pi l_B^2)$ [3,37] assuming that the Landau level filling factor ν remains everywhere close to 1 (see details in Appendix A). The above equation forms the basis of our transfer matrix analysis.

B. Real-space discretization of topological charge from geodesics

To calculate magnon transmission coefficients through the skyrmion crystal we need to discretize the energy functional in Eq. (11) on a finite grid, and hence in turn we need to discretize the exchange and the topological charge density terms. Discretizing the exchange term is a standard exercise in finite difference methods (see Appendix F); however, discretizing the variation in the topological charge density is a highly nontrivial task. Here we present an geometrical approach based on solid angles between geodesics. Such a discretization procedure should carry over for similar settings in metallic magnets hosting skyrmion crystals and could be transferred to other topological spin textures.

We associate a topological charge to each plaquette with the topological charge density being equal to to the solid angle subtended by the four spin vectors associated with the vertices of the plaquette. Before calculating the variation of such a solid angle, let us first consider the much simpler problem of the variation of the solid angle subtended by two spin vectors on the sphere with spherical coordinates (θ, ϕ) and $ds^2 = (d\theta)^2 + \sin^2 \theta (d\phi)^2$. The path between the end points of the two spin vectors $\hat{n}_1$ and $\hat{n}_2$ on the sphere describes a geodesic and the fluctuations in these spin vectors due to the spin waves describe a new geodesic; hence, the problem reduces to finding the variation in solid angle between these two geodesics, as shown in Fig. 7(a). The standard equations of motion for geodesics are

$$\ddot{\theta} = \frac{1}{2} \sin(2\theta) \dot{\phi}^2,$$
$$\sin^2 \theta \dot{\phi} = \text{const.} \qquad (14)$$

Without loss of generality (due to rotational invariance) we can choose $\boldsymbol{n}_0$ and $\boldsymbol{n}_1$ along the equator, so the corresponding geodesic becomes

$$\theta(t) = \pi/2; \quad \phi(t) = \phi(0) + (\phi_1 - \phi_0)t. \quad (15)$$

Considering the first-order variations in Eq. (14) we get

$$\delta\ddot{\theta} = \cos(2\theta)\dot{\phi}^2\delta\theta + \sin(2\theta)\dot{\phi}\,\delta\dot{\phi},$$
$$\sin(2\theta)\dot{\phi}\,\delta\theta + \sin^2\theta\,\delta\dot{\phi} = \text{const.} \quad (16)$$

Focusing on the vicinity of geodesic we get

$$\delta\theta = \frac{\delta\theta_0\sin(\alpha(1-t)) + \delta\theta_1\sin(\alpha t)}{\sin\alpha},$$
$$\delta\phi = \delta\phi_0(1-t) + \delta\phi_1 t, \quad (17)$$

where $\alpha = \phi_1 - \phi_0$.

In a radial gauge $\mathcal{A} = a(\theta)d\phi$. This $\mathcal{A}$ is actually a one-form on the unit sphere whose curl gives the solid angle, not to be confused with $\boldsymbol{A}$, which is the vector potential defined in real space (a vector). The solid angle between two parallel circles at θ and $\theta = d\theta$ is equal to $2\pi\sin\theta d\phi$ and should be equal to (via Stokes' formula) $2\pi(a(\theta + d\theta) - a(\theta))$, therefore $\frac{da}{d\theta} = \sin\theta$. We require that $a = 0$ as $\theta = 0$, hence $a(\theta) = 1 - \cos(\theta)$. The first-order variation in $\delta\Omega$ is equal to $\oint\mathcal{A}$ along the closed path formed by the parallelogram with vertices as the four spin vectors (2 bare and 2 perturbed) and is given by

$$\delta\Omega = \int_0^1\left[(1 - \cos(\theta + \delta\theta(t)))\frac{d(\phi + \delta\phi(t))}{dt}\right.$$
$$\left. - (1 - \cos\theta)\frac{d\phi}{dt}\right] + \delta\phi_0 - \delta\phi_1, \quad (18)$$

which after a bit of algebra can be written as

$$\delta\Omega = \frac{1 - \cos\alpha}{\sin\alpha}(\delta\theta_0 + \delta\theta_1). \quad (19)$$

To connect the above formula with the original spin vectors $\boldsymbol{n}_0$ and $\boldsymbol{n}_1$ we can also write the first-order variation as

$$\delta\Omega_{01} = -\frac{\boldsymbol{n}_0 \times \boldsymbol{n}_1}{1 + \boldsymbol{n}_0 \cdot \boldsymbol{n}_1}(\delta\boldsymbol{n}_0 + \delta\boldsymbol{n}_1), \quad (20)$$

where we have defined the z axis such that $\boldsymbol{n}_0 \times \boldsymbol{n}_1 = \sin\alpha\,\hat{z}$, with $\alpha \in [0, \pi]$ and $\cos\alpha = \boldsymbol{n}_0 \cdot \boldsymbol{n}_1$, which in turn also implies that $\delta\theta_i = -\delta\boldsymbol{n}_i \cdot \hat{z}$

To tackle the problem of discrete $\int\delta Q^2$ we consider all four plaquettes connected to a particular site 0. The variations in the solid angle and hence the topological charge density term that appears in the energy functional of Eq. (A4) has the form

$$\delta E_C^{(0)} = \sum_{0\in\square}\delta\Omega_\square^2. \quad (21)$$

On a plaquette with vertices $i, j, k,$ and l in anticlockwise order $\delta\Omega_{ijkl} = \delta\Omega_{ij} + \delta\Omega_{jk} + \delta\Omega_{kl} + \delta\Omega_{li}$ with each term being given by Eq. (20). Expanding these above terms and keeping only terms including the vertex 0 we get [see Fig. 7(b)

for vertex numbering]

$$\delta E_C^{(0)} = \delta\Omega_{01}^2 + \delta\Omega_{03}^2 + \delta\Omega_{05}^2 + \delta\Omega_{07}^2 + \delta\Omega_{01}\delta\Omega_{30}$$
$$+ \delta\Omega_{03}\delta\Omega_{50} + \delta\Omega_{05}\delta\Omega_{70} + \delta\Omega_{07}\delta\Omega_{10}$$
$$+ (\delta\Omega_{01} + \delta\Omega_{30})(\delta\Omega_{12} + \delta\Omega_{23})$$
$$+ (\delta\Omega_{03} + \delta\Omega_{50})(\delta\Omega_{34} + \delta\Omega_{45})$$
$$+ (\delta\Omega_{05} + \delta\Omega_{70})(\delta\Omega_{56} + \delta\Omega_{67})$$
$$+ (\delta\Omega_{07} + \delta\Omega_{10})(\delta\Omega_{78} + \delta\Omega_{81}). \quad (22)$$

We can view the above complicated expression in a tight-binding formulation, which will help us for the transfer matrix formalism. The first two lines in Eq. (22) include the on-site energy terms, all the lines include nearest-neighbor-hopping terms and the last two lines include second-nearest-neighbor-hopping terms. While on-site and nearest-neighbor terms also arise in the exchange part of the functional (see Appendix F), second-nearest-neighbor contributions come only from the variation in the topological charge density.

C. Recursive transfer matrix approach to calculate magnon transmission

In the previous two sections, we have set up the machinery needed to discretize the ferromagnet-skyrmion crystal-ferromagnet quantum Hall junction problem on a real-space grid. Now, to numerically obtain the transmission properties of an incoming magnon from the left ferromagnetic end and outgoing on the right end [as in Fig. 1(a)], one needs to perform either a recursive transfer matrix or recursive Green's function calculation. For transfer matrices, one usually recursively calculates the full transfer matrix of the system by multiplying matrices column by column and then performing a rotation to obtain transmission and reflection matrices [39]. For Green's functions one does the same procedure and then arrives at the conductivity using the Fisher-Lee relation [40,41]. However, both these problems suffer from numerical instabilities due to the presence of (growing) evanescent modes, which cause the product matrix to blow up. This instability is common also in the optics community, where one discretizes Maxwell's equations on a real-space lattice. In this section, we adapt a method proposed by Pendry [34] for the optics problem, to obtain the full transmission and reflection matrices of the problem despite the instability. All our transmission and reflection matrices, unless explicitly mentioned, are for a wave entering from the left and exiting on the right.

To calculate the magnon transmission across the junction we discretize the unit cell of size $a \times a$ into N slices in the x and the y direction. We then consider a semi-infinite strip of unit-cell width along the y direction and impose periodic boundary conditions along y. Now, consider a magnon entering the skyrmion crystal region with incident energy ω, transverse momentum q_y, and parallel momentum q_x, which are related by the standard ferromagnetic dispersion. Using the discretization procedure for the energy functional in Eq. (11), we can recast the resulting time-dependent Schrödinger equation (13) as a tight-binding equation, which in turn can be written as a matrix equation of the form

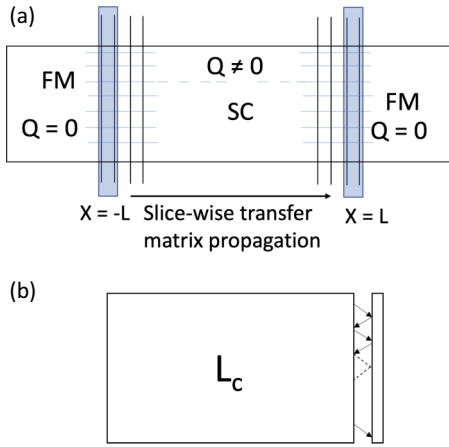$$D\Psi_X + A_R\Psi_{X+1} + A_L\Psi_{X-1} = 0, \quad (23)$$

FIG. 8. (a) Slice-wise recursive transfer matrix procedure for the ferromagnet-skyrmion crystal-ferromagnet junction. The solid lines highlight the real-space discretization and their intersection points are the lattice sites. (b) Multiple scattering processes for propagating transmission and reflection matrices. Calculate the transfer matrix for the slab of length L_c the usual way and then do successive slice-wise rotation to propagate the transmission matrices using the infinite series.

where $\Psi_X = (\chi(X,1), \bar{\chi}(X,1), ..., \chi(X,N), \bar{\chi}(X,N))^T$ is a column vector for all the χ, $\bar{\chi}$ with $x = X$ and the $2N \times 2N$ matrices, D, A_R, and A_L are matrices of coefficients for the wavefunctions at column X, $X+1$, and $X-1$ respectively (see Appendix A and Sec. IV A for expressions for χ and $\bar{\chi}$ and Appendix F for expressions for matrix elements). Such an equation can then be recast as a transfer matrix equation

$$\begin{bmatrix} \Psi_{X+1} \\ \Psi_X \end{bmatrix} = \hat{T}_X \begin{bmatrix} \Psi_X \\ \Psi_{X-1} \end{bmatrix},$$

$$\hat{T}_X = \begin{bmatrix} -A_R^{-1}D & -A_R^{-1}A_L \\ \mathbb{1} & 0 \end{bmatrix}, \quad (24)$$

where $\hat{T}_X$ is the $4N \times 4N$ transfer matrix, which relates the values of χ in the nearest-neighboring columns. Using the standard properties of transfer matrices we can propagate the wavefunction from the left ferromagnet region at $x = x_L$ through the skyrmion lattice to the right ferromagnet region at $x = x_R$, column by column, resulting in the final equation

$$\begin{bmatrix} \Psi_{x_R+1} \\ \Psi_{x_L} \end{bmatrix} = \hat{T} \begin{bmatrix} \Psi_{x_L+1} \\ \Psi_{x_L} \end{bmatrix},$$

$$\hat{T} = \prod_{i=x_L}^{x_R} \hat{T}_i. \quad (25)$$

Since in Sec. III we use truncated theta functions to smoothly interpolate between zero topological charge regions on the two ends and a finite periodic topological charge in the middle, we do not have sharp boundaries between the three separate regions. Hence we start our transfer matrix procedure on the left from a column in the region with zero topological charge density and we end on a slice on the right, again deep in the region, with zero topological charge density as shown in Fig. 8(a).

The transfer matrix procedure as illustrated relates the values of the wavefunctions of the two end-point columns and

not the amplitudes we need to calculate the transmission and reflection coefficients. To convert such a transfer matrix in the tight-binding formulation to the transfer matrix, which relates the amplitudes of the waves in the left region to those in the right, we first need to express the wavefunction in terms of these amplitudes using the standard scattering ansatz. For the wavefunction in the starting column at $x = x_L$, we can write

$$\chi_{x_L,y} = \sum_{i=1}^{N} A_{i'} e^{iq_{xi}x_L + iq_{yi}y} + B_{i'} e^{-iq_{xi}x_L + iq_{yi}y},$$

$$\bar{\chi}_{x,y} = \sum_{i=1}^{N} A_{i''} e^{iq_{xi}x_L + iq_{yi}y} + B_{i''} e^{-iq_{xi}x_L + iq_{yi}y}, \quad (26)$$

where $i' = 2i - 1$ and $i'' = 2i$, and q_{xi}, q_{yi} are the wavevectors of the N different modes, with $\triangle q_y = 2\pi/a$. Note here that generally, $\chi_{x_L} \neq \bar{\chi}_{x_L}^*$, even though $\chi = \chi_1 + i\chi_2$ and $\bar{\chi} = \chi_1 - i\chi_2$, because $\chi_1, \chi_2 \in \mathbb{C}$ as a result of complex phase factors (further details on this are given in Appendix I). Using the form of the scattering ansatz we can define the following rotation relating the $4N$ sized column vectors:

$$[\Psi_{x_L}, \Psi_{x_L-1}]^T = [\chi_{x_L,1}, ..., \bar{\chi}_{x_L-1,N}]^T$$
$$= Q_{x_L}[A_1 e^{ik_{x1}}, A_2 e^{ik_{x1}}, ...,$$
$$B_{2N-1} e^{-ik_{xN}}, B_{2N} e^{-ik_{xN}}]^T, \quad (27)$$

where Q_{x_L} is a $4N \times 4N$ matrix and k_{xi} and k_{yi} are the different modes obtained from the discretization on the grid, $k_{yi} = k_{y0} + 2\pi i/N$, with $i = 0, .., N-1$ and $k_{xi} = \omega/(2N^2)(2 - \cos(k_{yi}))$. These wavevectors on the grid are related to the continuous ones by $q_y a = k_y N$. We can then express the transfer matrix equation (25) in terms of the scattering amplitudes on both ends as

$$\begin{bmatrix} C_1 e^{ik_{x1}} \\ C_2 e^{ik_{x1}} \\ . \\ . \\ D_{2N-1} e^{-ik_{xN}} \\ D_{2N} e^{-ik_{xN}} \end{bmatrix} = \tilde{T} \begin{bmatrix} A_1 e^{ik_{x1}} \\ A_2 e^{ik_{x1}} \\ . \\ . \\ B_{2N-1} e^{-ik_{xN}} \\ B_{2N} e^{-ik_{xN}} \end{bmatrix},$$

$$\tilde{T} = Q_{x_R}^{-1} T Q_{x_L} \quad (28)$$

where C_i, D_i represent the amplitudes for the wavefunction on the rightmost slice at $x = x_R$. The transmission and reflection coefficients can be expressed from the elements of the rotated transfer matrix $\tilde{T}$, see Eq. (30).

Such a columnwise multiplied transfer matrix procedure runs into numerical instabilities due to growing evanescent modes, which blow up on increasing the length of middle region (largest eigenvalue >1) and are a common cause of instability in such recursive transfer matrix methods. To overcome this we use a method common in optics [34], in which one uses the usual recursive approach up to a certain column and then propagates the transmission and reflection matrices columnwise thereon using multiple scattering, instead of propagating the whole transfer matrix, as shown in Fig. 8(a). Such an approach does not suffer from numerical instabilities since the reflection and transmission matrices are bounded because of unitarity of the scattering matrix. To obtain the transmission and reflection matrices for a slab of length L_c,

we perform the rotation shown above to obtain

$$Q_{L_c}^{-1} T_{L_c} Q_0 = \tilde{T}_{L_c} = \begin{bmatrix} \tilde{T}_{L_c 11} & \tilde{T}_{L_c 12} \\ \tilde{T}_{L_c 21} & \tilde{T}_{L_c 22} \end{bmatrix}, \qquad (29)$$

where T_{L_c} is the transfer matrix obtained relating the columns at the two ends of the slab of length L_c and Q is the rotation matrix as defined earlier. One can obtain the transmission matrices $Tr(L_c)$ and $R(L_c)$ for the slab from the $\tilde{T}_{Lcij}$. They are given by

$$R(L_c) = -\tilde{T}_{L_c 22}^{-1} \tilde{T}_{L_c 21},$$
$$\text{Tr}(L_c) = \tilde{T}_{L_c 11} + \tilde{T}_{L_c 12}^{-1} R(L_c), \qquad (30)$$

where $\tilde{T}_{L_c ij}$, $i, j \in [1, 2]$ are the $2N \times 2N$ blocks in Eq. (29). Say we have a situation in which we calculate the transmission and reflection matrices, $Tr(L_c)$ and $R(L_c)$ for a slab of length (L_c) within numerical accuracy using the standard recursive protocol. We can then propagate the transmission and reflection matrices by summing up the infinite series from multiple scattering events from the additional slice, as shown in Fig. 8(b), to get

$$\text{Tr}(L_c + 1) = \text{Tr}(1)(I - T_1 R(1))^{-1} \text{Tr}(L_c),$$
$$R(L_c + 1) = R(L_c) + T_2 R(1)(I - T_1 R(1))^{-1} \text{Tr}(L_c), \quad (31)$$

where $\text{Tr}(1)$ and $R(1)$ are the transmission and reflection matrices for a wave incident from the left on the added slice, obtained using the same procedure as in Eqs. (29) and (30) [but now with $T(1)$ instead of T_{Lc}]. T_1, T_2 are the reflection and transmission matrices for a wave incident from the right on the slab of length L_c respectively [34]. Such an approach, although more numerically expensive due to more matrix inversions, resolves the numerical instabilities and allows one to calculate the full transmission and reflection matrices.

V. MAGNON TRANSMISSION THROUGH A SKYRMION CRYSTAL

Using the technical advancements described in Secs. V A–V C, one can numerically solve the scattering problem of magnon scattering in the ferromagnet-skyrmion crystal-ferromagnet setup. The main results of the problem provide a unique set of transport signatures for the skyrmion crystal. They are summarized in the Sec. II and in Figs. 1(c) and 1(d). In this section we provide some additional results of the scattering problem that reflect the topology-symmetry dichotomy.

With the detailed analysis of our heuristic model of a particle scattering in a magnetic field in hand, we return to the full problem of the ferromagnet-skyrmion crystal energy functional in Eq. (11). As pointed out earlier, the effect of a nonzero coupling constant in the topological charge density term is to provide some sense of stiffness to the skyrmion crystal, and thereby inducing dispersion in the Goldstone modes. To separate the dispersion effect first we look at the $g = 0$ case in which all Goldstone modes are pinned to zero and the Riemann-Goldstone Landau level is a zero-energy flat band. From the full expression of the variation of the energy functional in Eq. (12), one can see that for $g = 0$ the expression resembles that of the heuristic model, as explained in Sec. IV A. Hence, we can use the intuitive understanding developed in Sec. III.

A. Similarities with heuristic picture—High-energy sector

For $g = 0$, based on our transfer matrix analysis, we see that the transmission spectra in Fig. 9(c) reflects the underlying topology of the skyrmion crystal, since the nonzero transmission occurs in energy regions, which reflect the emergent Landau levels of the problem. We also note the remarkable qualitative similarity of the response with that of the heuristic model in Figs. 4(a) and 4(b). For two skyrmions in a unit cell, we get four flux quanta acting on a spin-1 magnon, which justifies our use of the analogous average magnetic field $B_0 = 8\pi/a^2$ for the results in Figs. 4(a) and 4(b) (see Appendix A and [42]). We see that the transmission peaks are suppressed, i.e., we do not get full transmission at these resonant energies, and one can understand this using similar multichannel interference arguments presented in Appendix E for the heuristic model.

Besides calculating transmission coefficients we also obtain the spectra for the skyrmion crystal from the energy functional in Eq. (11). For the $g = 0$ "skyrmion crystal", we find that the high-energy modes resemble the dispersive Landau levels, similar to those observed in the heuristic model for a spatially varying magnetic field. The transmission peaks occur in energy regimes of the effective Landau levels and the gaps in nonzero transmission correspond exactly to the gaps in the Landau level dispersion.

The qualitative similarity with the heuristic model also implies that magnon transmission at high energies will be characterized by certain preferred angles of transmission and a nonmonotonic dependence of transmission on the channel momenta. Such a nonmonotonic dependence on channels and corresponding angular spread is a clear consequence of crystalline order.

B. Effects of Goldstone mode dispersion—Low-Energy sector

The lowest-energy modes for the $g = 0$ case are pinned to zero energy since one can deform $\boldsymbol{n}_0(\boldsymbol{r})$ continuously in the space of holomorphic textures while keeping the exchange energy constant [first term in Eq. (11)]. Hence, for $g = 0$ we get localized modes in the Riemann-Goldstone Landau level. On introducing a finite g, we see from the Goldstone mode spectra in Fig. 9(b) that the Goldstone modes acquire a finite dispersion. We get three low-energy Goldstone modes, as expected for an SU(2) skyrmion crystal. Out of these three, two modes are almost degenerate and have a higher velocity than the third. All these modes have a linear dispersion at low q, as behooves an antiferromagnet. Note that remarkably, one can infer all this information about the Goldstone modes just by looking at the transmission spectra in Fig. 9(a). We see that there are two sets of peaks, within each set, the peaks are equally spaced and increase in height on increasing energy.

Such behavior is qualitatively consistent with our results from the heuristic model of the ferromagnet-antiferromagnet-ferromagnet junction [see Fig. 6(b)]. These two sets of peaks correspond to the two Goldstone mode branches, and their different peak positions imply that the velocity of these two modes are different, as verified by our results of the Goldstone mode spectrum in Fig. 9(b). We also see that there is a very small splitting in one set of peaks, indicating the fact that the two higher-velocity modes are almost degenerate.
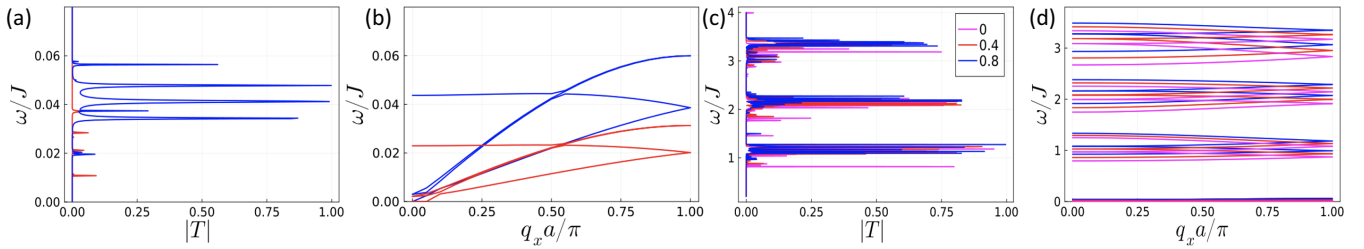
FIG. 9. Transmission and energy spectra for the ferromagnet-skyrmion crystal-ferromagnet junction at normal incidence $q_y = 0$ at g/J = 0.4 (red), 0.8 (blue), and 0 [magenta, only in (c), (d)]. The effect of increasing g in the second term of the energy functional in Eq. (11) on (a) low-energy transmission, peaks shift and increase in height (b) Goldstone mode dispersion, modes become more dispersive and (c) high-energy transmission, slight shift in position of peaks but no significant change in height (d) High-energy dispersion, slight shift in energy.

On increasing g, we see that the Goldstone modes become more dispersive, as in Fig. 9(b) and one can also infer this by looking a the transmission spectra, the peaks of which shift and become more prominent, as in Fig. 9(a).

Hence, the magnon transmission spectra encode the nature of the Goldstone mode spectra in the emergent Riemann-Goldstone Landau level sector of the skyrmion crystal.

We also note from Fig. 9(d) that the peaks in the higher-energy effective Landau levels are slightly shifted but the heights are relatively unaffected on increasing g, which confirms that the physics of the Riemann-Goldstone Landau level, associated with symmetry breaking, is indeed distinct from that induced by the underlying topology of the spin texture. Such separation of energy scales highlights the topology-symmetry dichotomy of the problem and is very nicely elucidated by the magnon transmission. Moreover, the qualitative similarities of the two heuristic models with the two different energy sectors also presents a simplified and intuitive understanding of this very rich problem.

We note that the Goldstone modes present in Fig. 9(b) do not go down to exactly zero energy. This is a consequence of real-space discretization and the holomorphic ansatz being an exact minimum of the exchange terms only in the continuum limit. Because of this, for a finite discretization scheme, the Goldstone mode eigenvalues will actually have a small imaginary part (compared to the real part). We have plotted only the real part of these eigenvalues in Fig. 9(b). However, as we approach the continuum limit, the ansatz exactly minimises the energy and so for larger values of N, the complex part becomes numerically insignificant and the real part of the modes will go down to exactly 0 as $q \to 0$ in Fig. 9(b). The phonon mode in our low-energy spectra, however, shall remain gapped due to the nature of our energy functional: the spatial modulations of the topological charge density $Q_0(\mathbf{r})$ explicitly break translational symmetry. This gapped phonon branch appears as the upper branch in Fig. 9(b). We comment more on the implications and feasibility of the gapped magnetophonon in the next section.

VI. DISCUSSION

A. Anisotropies and experimental considerations

In this paper we have used an effective continuous model derived from a holomorphic ansatz motivated from the physics of isotropic skyrmion crystals. This approach carries a long way in terms of physical intuition, analytical control, and a full qualitative understanding from such an effective theory. However, there are features beyond the model that could be present in experiment. In this section, we discuss how such features could modify the results we presented. Just as importantly, we also discuss how the results from our model could be realized in ongoing experiments.

The price we pay for using the holomorphic ansatz as a starting point is the absence of anisotropies. While the energy scale for anisotropies is smaller than that of the Coulomb interaction, they still play a role in the low-energy physics of monolayer graphene in the zeroth Landau level [43]. The leading anisotropy in such systems would be the Zeeman term $g_1 \mu_b \mathbf{n} \cdot \mathbf{B}$. The dispersion for realistic models of skyrmion crystals in graphene with such terms were studied in [23] using Hartree-Fock methods. The authors showed that the Zeeman term gaps out one of the three Goldstone modes. Hence, we expect that the transmission signatures we predict for the Goldstone modes can still be observed in experiments on monolayer graphene, with the modification that the spacing of the peaks would be less linear in the low-energy sector of the transmission spectra. The higher-energy signatures from the effective Landau levels should also be robust to the presence of any relevant anisotropies such as the Zeeman, or even the lattice scale, terms. We also note, as briefly mentioned in the section above, due to our energy functional being constructed to have our truncated theta-function ansatz as the minima, the magnetophonon mode obtained from our spectra in Fig. 9(b) is also gapped. In isotropic and fully periodic skyrmion crystals such a mode is expected to be gapless and have the characteristic $\sim q^2$ dispersion for short range and $q^{3/2}$ dispersion for Coulomb interactions in two dimensions [24]. However, one nonetheless expects the phonon mode to be gapped in the presence of the junction between regions of different filling. Moreover, anisotropies also gap out the phonon mode [23], hence we do not expect its presence to alter our results much. Besides anisotropies, there could also be some positional distortion of the skyrmions arising from background charges. One of the advantages of the formulation of our theta function ansatz is that we could very well construct an alternative ansatz, which has an irregular structure along the parallel direction (x axis). However, if we completely loose periodicity along the transverse direction (y axis), then the scattering problem would be much harder to solve numerically.

Another source of potential mismatch between experiment and our theory would be the range of our interaction term.

The interaction term in our effective energy functional is a delta function (in real-space) terms, whereas the Coulomb interaction is long range. However, such an interaction can be engineered in graphene using metallic gates, which screen the Coulomb interaction. A typical magnon transport experiment on graphene involves a sheet of monolayer graphene sandwiched in between hBN substrates and additional metallic gates on top and bottom. The gate-screened potential in momentum space is given by

$$V(q) = \frac{4\pi e^2}{\sqrt{\epsilon_x \epsilon_z}} \frac{\sinh\left(qd\sqrt{\frac{\epsilon_x}{\epsilon_z}}\right) \sinh\left(qd'\sqrt{\frac{\epsilon_x}{\epsilon_z}}\right)}{q \sinh\left(q(d+d')\sqrt{\frac{\epsilon_x}{\epsilon_z}}\right)}, \quad (32)$$

where d and d' are the distance from the top and bottom gates to the graphene sample and ϵ_x, ϵ_z are the static in and out-of plane permittivites of the hBN [44]. On tuning the parameters d and d', it is plausible to expect that one can realize a potential structure that is fairly flat in momentum space, leading to a localized delta function in real space. Moreover, by tuning the strength of the interaction, one can also tune the coupling constant g, which controls the dispersion of the Goldstone modes and hence one can observe the variations in the transmission spectra as mentioned in the previous section.

For current experiments on graphene, the external field $B_{\text{ext}} \sim 10T$, hence $l_B \sim 10$ nm. In our model, we assume that all spatial variations are on scales larger than the magnetic length. In particular, the two important scales are the skyrmion crystal lattice constant and the interface width, governed by electrostatics. In our ansatz these two length scales are comparable. Hence, to exactly derive results from our model for experiment, these two length scales should be at least an order of magnitude larger than l_B. If, in experiments the skyrmion period is of the order of l_B, or if the ferromagnet-skyrmion crystal interface is much sharper then one might need to resort to more microscopic time-dependent Hartree-Fock treatments, which will likely change some quantitative details, but should retain the structure of transmission from Goldstone modes in the Riemann-Goldstone Landau level and higher-energy effective-Landau levels presented here. Such qualitative similarity is fair to expect for low momentum physics given the early work on skyrmions, which compared Hartree-Fock and effective continuous theory treatments [3,4,37,45], and is also bolstered by the qualitative similarities between our heuristic model for the ferromagnet-antiferromagnet junction and a full Hartree-Fock calculation for the junction with $\nu = 0$ sandwiched in the middle [36].

In our model, for theoretical purposes, the effective Landau level gap is $\sim J$, the exchange coupling constant. However, we can estimate what this effective gap $\hbar\omega_G$ will be in experiment. To do so we neglect the g terms since as we have seen in the last section they only have a qualitative effect on the Goldstone modes. Now, we can use the similarity with the heuristic model in Sec. III, to consider a magnetic field $B = 4\pi Q_0$ with $Q_0 = \delta\nu/(2\pi l_B^2)$ where $\delta\nu$ is the deviation from unit filling in the central region. The spectral gap for the simplified energy functional is $2JB$. Using Eq. (13), we get $\alpha\omega_G = 4JB$. Using the values of α and B we can write $\hbar\omega_G = 32\pi J\delta\nu$. Now using the standard value of $J = e^2/(32\sqrt{2\pi}\epsilon l_B)$ we obtain a

spectral gap $\hbar\omega_G = \sqrt{\frac{\pi}{2}} \frac{e^2}{\epsilon l_B} \delta\nu$. The gap is linear in $\delta\nu$. This is important as $\delta\nu$ is easily tunable in experiment.

The experimental detection of our transmission signatures would in principle require knowledge of the incoming magnon energy distribution. There has been experimental progress in this direction. For example, in the Supplement of [17], the authors use noise measurements to infer the Poissonian distribution of the magnon energies. Furthermore, as seen in [36], one can use the incidence angle as an energy filter for magnons. To obtain detailed information about the energy distribution of such magnons one would need to know in detail the mechanism behind magnon emission and absorption from quantum Hall devices, which depend on edge state physics [14]. Fortunately, there is no edge state reconstruction physics in graphene [46] and hence we think this is an achievable task. However, the energy resolved measurement of transmission is still an experimental limitation and we hope our paper will motivate experimental advances in this direction.

The experiment in [22], which was part of our motivation for this project, prepared a junction similar to the one suggested in our paper and reported the observation of a possible skyrmion crystal due to suppression of transmission on doping slightly away from $\nu = 1$ in the central region. At such a filling of the central region, theoretically one would expect the formation of a skyrmion crystal [4], which has a qualitatively different Goldstone mode dispersion compared to the ferromagnet, and the observed suppression would agree with the picture of magnon decay into some of these. This experiment raised the important question of the nontrivial interaction between ferromagnetic magnons and excitations with qualitatively different dispersions.

While consistent with the hypothesis of the formation of the skyrmion crystal, the reported suppression does not tell us much about the nature of its Goldstone/high-energy modes. Moreover, such suppression can also arise within the context of elastic scattering, due to any other spin structure, which hosts a qualitatively different dispersion as compared to the incoming magnon; for example, similar suppression is seen for the case of the ferromagnet-antiferromagnet junction (Sec. III and [35,36]). Our results provide concrete signatures in nonlocal response, which are unique to the skyrmion crystal and as far as we can see do not appear in any other phase in the quantum Hall phase diagram. The combination of Landau-level like transmission and equally spaced low-energy peaks due to the linear nature of the Goldstone modes would elucidate both the degree of crystalline order and the nature of the skyrmion crystal. Further experiments in which the nonlocal response is studied as a function of the incoming magnon energy should be able to detect such signatures.

B. Outlook

We have shown how magnon transport through skyrmion crystals probes the interplay of topology and symmetry breaking. We have shown that the magnon transmission spectra allows one to probe the topology arising from the high-energy effective Landau level structure, which comes from the texture of skyrmion crystal. Moreover, and perhaps more interestingly, low-energy transmission spectra can also probe the nature of the Goldstone modes in the Riemann-Goldstone

Landau level, which arises from a complex interplay of the topology as well as SU(2) symmetry breaking. Therefore, not only does our paper provide a rich example of the salient features of the confluence of topology and symmetry breaking, it also presents a set of results, which allow one to probe crystalline order and map out the excitation spectrum of a quantum Hall skyrmion crystal—direct experimental evidence of which has not been established conclusively—in current ongoing experiments.

We have also provided a simpler tool set comprising two heuristic models, which allow us to intuitively understand parts of the complex problem. Moreover, to solve the complex problem, we have made several technical advances, which are easily transferable to analogous problems elsewhere. Firstly, we have provided an analytical framework to study junctions of topologically trivial and nontrivial structures. Secondly, we have provided a novel method for the discretization of topological charge in real space, of possible use in various fields, including metallic magnets. Thirdly, inspired from optics literature, we have provided a recursive method to numerically obtain full transmission and reflection matrices for generic scattering problems despite having instabilities due to evanescent contributions. An alternate way to approach such a scattering problem, especially for the Goldstone mode sector would be to construct long-wavelength sigma model descriptions of such junctions. However, such a problem is complicated by the different order parameter manifolds of the ferromagnet and skyrmion crystal. In Appendices J and K we have also provided an example of the construction of a type of nonlinear sigma model for such a junction-like structure between two different ground-state manifolds. Such a construction and its extensions can also be used in metallic magnets, where two magnetic materials with different collective excitations are separated by domain walls. We have kept this for the Appendix as it does not directly relate to the rest of the content and is more a step for future works.

Besides monolayer graphene, where quantum Hall skyrmion crystals are expected to form near unit filling of the zeroth Landau level, there are various other platforms, which host skyrmion crystals. Metallic magnets in two and three dimensions, for example, as mentioned in the main text have been a rich source of skyrmion crystal physics. Besides these usual suspects, with the advent of twistronics, spurred by the experiments on twisted bilayer graphene [47,48], there have been several proposals for the realization of skyrmion crystal phases in such settings. For example, in twisted bilayer graphene, skyrmions have been proposed as the lowest-energy charged excitations of the insulating phase, and possibilities of such skyrmions forming a crystal have also been put forward [49–52]. Also, a recent experiment in twisted bilayer graphene has used SQUID measurements to map out the inhomogeneous spatially varying Berry curvature-induced magnetism at zero external field [53] near the magic angle. While we have considered periodically varying effective magnetic fields in our problem, one could extend this to incorporate disordered profiles. Such profiles should have a distinct signature in the magnon response. Hence, our paper motivates the possibility of the exploring the zero-field Chern mosaic in twisted bilayer graphene using magnon transport. Besides graphene,

skyrmion crystal phases have also been proposed in other twisted van der Waals magnets [54,55]. Our paper presents a route to detect skyrmion crystals in all these systems using magnon scattering.

One can also use our analytical ansatz to formulate the scattering problem for other topologically nontrivial structures such as meron or bimeron crystals [56]. Meron crystals have a different collective mode dispersion [23], hence it would be interesting to see how their transport signatures differ for magnon scattering. Most of the theoretical work thus far has focused on integer fillings in the central region. One could also ask the question of what response ground states of fractional fillings have in such magnon scattering. Our analytical ansatz of the theta functions, as mentioned in the main text, is closely related to the analytic part of the Laughlin-Jastrow wavefunctions under periodic boundary conditions [38]. Hence using such truncated versions of similar holomorphic functions could be a good starting point for such a theoretical analysis. Moreover, fractionally charged skyrmions have also been predicted near certain fractional fillings [57–60], and similar suppression of the nonlocal response as for integer charged skyrmion crystals was also observed [22]. Hence, studying their response and comparing with our results would be an interesting direction to pursue.

Another avenue of theoretical research would be to explore the scattering problem for crystals of entanglement skyrmions. Entanglement skyrmions are textured of entangled spin-valley degrees of freedom [33]. A recent paper has shown that such skyrmions could be realized in monolayer graphene under realistic values of anisotropies [61]. It would be interesting to explore if the injection of spin waves could detect the degree of entanglement between spin and valley degrees of freedom. The nonlinear sigma model construction shown in this paper would also be a much richer theoretical problem for the entangled skyrmion case due to the entanglement skyrmions living in $\mathbb{C}P^3$ space.

Moreover, as also mentioned in the main text, the presence of effective Landau levels for the magnons presents such skyrmion crystals as a fertile platform for topological magnonics, a point appreciated also in a recent work of a skyrmion crystal in a three dimensional metallic magnet [27]. Such connections allow one to transfer the physics of Chern bands, edge states, and bulk-boundary correspondence from topological band theory to magnons. Besides quantum Hall junctions, such junction like structures have also been considered for domain walls in two-dimensional magnets [62,63]. Two-dimensional antiferromagnets host stable skyrmions [64] and recently, skyrmion domain walls between a ferromagnet and antiferromagnet have also been considered [30]. Hence, it would be interesting to study how the signatures of an antiferromagnetic skyrmionic crystal would differ from our results of a ferromagnetic one. Finally, another interesting question is the influence of magnon interactions or thermal fluctuations on this scattering problem; however, that is well beyond the current scope and we leave it for future work.

Given the angular dependence of the transmission predicted in our paper for magnon scattering off skyrmion crystals, several interesting experimental possibilities also emerge. One could create geometrically optimized junctions to maximize magnon transmission, and perhaps also place a

series of such junctions to create a narrow beam of magnons with very little angular spread.

Overall, the new experimental capacities are remarkably well suited to study phenomena arising from the combination of symmetry-breaking and topology in two-dimensional systems, and we hope this paper will motivate further studies of this complex of questions in both theory and experiment.

APPENDIX A: EQUATIONS OF MOTION AND MAPPING TO SCHRÖDINGER EQUATION

In this Appendix we provide the details of the spin-wave theory calculations starting from Eq. (11) in the main text. Due to our construction of the energy functional, we have seen that the holomorphic texture $|\psi(\mathbf{r})\rangle_0$ and hence $\mathbf{n}_0(\mathbf{r})$ forms a locally stable minimum, so we have a well-defined collective mode (magnon) spectrum for fluctuations around $\mathbf{n}_0(\mathbf{r})$.

We introduce small deviations such that $\mathbf{n}(\mathbf{r}, t) = \mathbf{n}_0(\mathbf{r}) + \delta\mathbf{n}(\mathbf{r}, t)$. First, we need to construct local coordinates $\chi_1(\mathbf{r})$ and $\chi_2(\mathbf{r})$ around $\mathbf{n}_0(\mathbf{r})$ on the sphere. To do so, we introduce local orthonormal frames $(\mathbf{n}_0, \mathbf{e}_1, \mathbf{e}_2)$ such that $\mathbf{n}_0(\mathbf{r}) = \mathbf{e}_1(\mathbf{r}) \times \mathbf{e}_2(\mathbf{r})$, using which we can write

$$\delta\mathbf{n}^{(1)}(\mathbf{r}) = \chi_1(\mathbf{r})\mathbf{e}_1(\mathbf{r}) + \chi_2\mathbf{e}_2(\mathbf{r}). \tag{A1}$$

Since $|\mathbf{n}(\mathbf{r}, t)|^2 = 1$, we get $\mathbf{n}_0(\mathbf{r}) \cdot \delta\mathbf{n}^{(1)}(\mathbf{r}, t) = 0$. To study collective modes, we need to expand the total energy to second order in $\chi_1(\mathbf{r})$ and $\chi_2(\mathbf{r})$. Normalizing $\mathbf{n}(\mathbf{r})$ and then expanding up to second order we get $\delta\mathbf{n} = \delta\mathbf{n}^{(1)} + \delta\mathbf{n}^{(2)}$, with

$$\delta\mathbf{n}^{(2)}(\mathbf{r}) = -\frac{1}{2}[\chi_1(\mathbf{r})^2 + \chi_2(\mathbf{r})^2]\mathbf{n}_0(\mathbf{r}). \tag{A2}$$

Now, by expanding $\partial_i \mathbf{n} \cdot \partial_i \mathbf{n}$ to second order and using the fact that $\mathbf{n}_0(\mathbf{r})$ is a local minimum of the energy functional we get the following expression for the energy functional:

$$E = E_0 + g \int \delta Q(\mathbf{r})^2 + J \int [\partial_x(\delta\mathbf{n}^{(1)})]^2 + [\partial_y(\delta\mathbf{n}^{(1)})]^2$$
$$- [(\partial_x\mathbf{n}_0)^2 + (\partial_y\mathbf{n}_0)^2](\chi_1(\mathbf{r})^2 + \chi_2(\mathbf{r})^2), \tag{A3}$$

where δQ is the first-order variation of the topological charge density. Using Eqs. (A2) and (A3) and the holomorphic constraint arising from minimizing the exchange energy at fixed topological charge, we can write the change in energy as

$$\delta E^{(2)} = g \int \delta Q(\mathbf{r})^2 + J \int \left[|i\partial_x\chi + A_x\chi|^2 + |i\partial_y\chi + A_y\chi|^2 \right.$$
$$\left. - (c_{1x}^2 + c_{2x}^2)|\chi|^2 \right] dx dy, \tag{A4}$$

where $A_{x/y} = \hat{\mathbf{e}}_1 \cdot \partial_{x/y}\hat{\mathbf{e}}_2$, $c_{1x/y} = \hat{\mathbf{e}}_1 \cdot \partial_{x/y}\mathbf{n}_0$, and $c_{2x/y} = \hat{\mathbf{e}}_2 \cdot \partial_{x/y}\mathbf{n}_0$. We find that the second-order variation of the exchange term can be interpreted as the energy of a quantum particle described by a wavefunction $\chi(\mathbf{r}) = \chi_1(\mathbf{r}) + i\chi_2(\mathbf{r})$, $\bar{\chi}(\mathbf{r}) = \chi_1(\mathbf{r}) - i\chi_2(\mathbf{r})$ and subject to a vector potential $\mathbf{A}$, an effective magnetic field $B = 4\pi Q_0$ and a scalar potential $c_{1x}^2 + c_{2x}^2$ (see Appendices B and C for more details on the effect of the holomorphic constraint and gauge invariance of the energy functional). The physical origin of this effective magnetic field, as mentioned earlier, comes from the Berry phase picked up by the magnon when traversing through the skyrmion crystal.

In order to get linear equations of motion we now expand the standard Landau-Lifshitz equations to first order in δn. Since $\delta E/\delta n = 0$ for the configuration $\mathbf{n}_0(\mathbf{r})$, the linearized version of the standard Landau-Lifshitz equations gives us

$$\alpha \frac{\partial}{\partial t}\delta n^a = \epsilon^{abc} n^b \frac{\delta E^{(2)}}{\delta \delta n^c}, \tag{A5}$$

where $\alpha = \hbar/(4\pi l_B^2)$, [3,37] assuming that the Landau level filling factor ν remains everywhere close to 1. Now, on using the equations derived in this section we can express the linearized equation in matrix form as

$$\alpha \frac{\partial}{\partial t} \begin{bmatrix} \chi_1 \\ \chi_2 \end{bmatrix} = \begin{bmatrix} 0 & -1 \\ 1 & 0 \end{bmatrix} \begin{bmatrix} \delta E^{(2)}/\delta\chi_1 \\ \delta E^{(2)}/\delta\chi_2 \end{bmatrix},$$
$$\alpha \frac{\partial \chi}{\partial t} = 2i\frac{\delta E}{\delta\bar{\chi}}, \tag{A6}$$
$$\alpha \frac{\partial \bar{\chi}}{\partial t} = -2i\frac{\delta E}{\delta\chi},$$

which is a time-dependent Schrödinger equation for the Bogoliubov-de Gennes-like energy functional E.

APPENDIX B: EFFECT OF HOLOMORPHIC CONSTRAINT

The holomorphic constraint results from minimizing the exchange energy at fixed total topological charge. Let us see how this arises. We denote $\mathbf{v}_x = \partial_x\mathbf{n}_0$ and $\mathbf{v}_y = \partial_y\mathbf{n}_0$, both of these quantities belong to the plane perpendicular to $\mathbf{n}_0$, so we can regard them as two-component vectors.

The exchange energy density is $\mathbf{v}_x^2 + \mathbf{v}_y^2$ and the local topological energy density is $1/(4\pi)\mathbf{v}_x \times \mathbf{v}_y = 1/(4\pi)J'(\mathbf{v}_x) \cdot \mathbf{v}_y = -1/(4\pi)\mathbf{v}_x \cdot J'(\mathbf{v}_y)$, where $J' = (0, -1; 1, 0)$. Let us minimize $\mathbf{v}_x^2 + \mathbf{v}_y^2$ at fixed $\mathbf{v}_x \times \mathbf{v}_y$, i.e., we extremize the function $(\mathbf{v}_x, \mathbf{v}_y) \to (\mathbf{v}_x^2 + \mathbf{v}_y^2)/2 - \lambda\mathbf{v}_x \times \mathbf{v}_y$, where λ is a Lagrange multiplier. We get

$$\mathbf{v}_x + \lambda J'(\mathbf{v}_y) = 0,$$
$$\mathbf{v}_y - \lambda J'(\mathbf{v}_x) = 0, \tag{B1}$$

which implies that $\mathbf{v}_x^2 + \lambda^2 J'^2(\mathbf{v}_x) = 0$ and $(1 - \lambda^2)\mathbf{v}_x = 0$, so $\lambda = \pm 1$. Since $\mathbf{v}_y = \lambda J'(\mathbf{v}_x)$ and $\mathbf{v}_x \times \mathbf{v}_y = \lambda J'(\mathbf{v}_x) \cdot J'(\mathbf{v}_x)$, $\lambda = 1(-1)$ implies a positive (negative) local topological charge density. In our case Q_0 is positive, therefore the holomorphic constraint corresponds to $\lambda = 1$. This implies $\mathbf{v}_y = J'(\mathbf{v}_x)$, so

$$\begin{pmatrix} c_{1y} \\ c_{2y} \end{pmatrix} = \begin{pmatrix} -c_{2x} \\ c_{1x} \end{pmatrix}, \tag{B2}$$

where $c_{(1/2)(x/y)} = \boldsymbol{e}_{(1/2)} \cdot \partial_{(x/y)}\boldsymbol{n}_0$ as in the main text. Therefore

$$Q_0(\boldsymbol{r}) = \frac{1}{4\pi}\boldsymbol{n}_0 \cdot (\partial_x\boldsymbol{n}_0 \times \partial_y\boldsymbol{n}_0)$$

$$= \frac{1}{4\pi}(c_{1x}c_{2y} - c_{1y}c_{2x})$$

$$= \frac{1}{4\pi}\left(c_{1x}^2 + c_{2x}^2\right). \tag{B3}$$

APPENDIX C: CHECKS FOR GAUGE-INVARIANCE

In our choice of local frames in the spin-wave theory calculations, we have gauge freedom. Instead of choosing $\boldsymbol{e}_1, \boldsymbol{e}_2$ we could also choose $\boldsymbol{e}'_1 = \cos(\lambda(\boldsymbol{r}))\boldsymbol{e}_1 + \sin(\lambda(\boldsymbol{r}))\boldsymbol{e}_2$ and $\boldsymbol{e}'_2 = -\sin(\lambda(\boldsymbol{r}))\boldsymbol{e}_1 + \cos(\lambda(\boldsymbol{r}))\boldsymbol{e}_2$. Then we would have

$$\begin{pmatrix} \chi_1(\boldsymbol{r}) \\ \chi_2(\boldsymbol{r}) \end{pmatrix} = \begin{pmatrix} \cos(\lambda(\boldsymbol{r})) & -\sin(\lambda(\boldsymbol{r})) \\ \sin(\lambda(\boldsymbol{r})) & \cos(\lambda(\boldsymbol{r})) \end{pmatrix}\begin{pmatrix} \chi'_1(\boldsymbol{r}) \\ \chi'_2(\boldsymbol{r}) \end{pmatrix},$$

$$\chi(\boldsymbol{r}) = e^{i\lambda(\boldsymbol{r})}\chi'(\boldsymbol{r}), \tag{C1}$$

where $\chi = \chi_1 + i\chi_2$ as in the main text. Under the gauge transformation above, $(c_{1x}, c_{2x})^T$ and $(c_{1y}, c_{2y})^T$ transform as $(\chi_1, \chi_2)^T$. The relations in Eqs. (B2) and (B3) expressing the holomorphic nature of $\boldsymbol{n}_0(\boldsymbol{r})$ are preserved under gauge transformations, since J' commutes with $R(\lambda)$ (the rotation matrix in the top line of the above equation). Now we look at the influence of a gauge transformation on the terms in the energy functional in Eq. (A4),

$$A'_x = \boldsymbol{e}'_1 \cdot \partial_x\boldsymbol{e}'_2 = \boldsymbol{e}'_1 \cdot (-\boldsymbol{e}'_1\partial_x\lambda - \sin(\lambda)\partial_x\boldsymbol{e}_1 + \cos(\lambda)\partial_x\boldsymbol{e}_2)$$

$$= -\partial_x\lambda + A_x, \tag{C2}$$

and the same result holds for A_y. Together with Eq. (C1) this implies that

$$\nabla\chi - i\boldsymbol{A}\chi = e^{i\lambda}(\nabla\chi' - i\boldsymbol{A}'\chi'), \tag{C3}$$

which ensures that the all the exchange terms in the energy functional are gauge invariant. To show the gauge invariance of the δQ terms let us first expand δQ to first order in $\delta\boldsymbol{n}^{(1)}$ [see Eq. (A1) for expression]. We can write

$$4\pi\delta Q = \delta\boldsymbol{n}^{(1)} \cdot (\partial_x\boldsymbol{n}_0 \times \partial_y\boldsymbol{n}_0) + \boldsymbol{n}_0 \cdot (\partial_x\delta\boldsymbol{n}^{(1)} \times \partial_y\boldsymbol{n}_0)$$

$$+ \boldsymbol{n}_0 \cdot (\partial_x\boldsymbol{n}_0 \times \partial_y\delta\boldsymbol{n}^{(1)}). \tag{C4}$$

The first term vanishes, since $\partial_x\boldsymbol{n}_0$ and $\partial_y\boldsymbol{n}_0$ are both orthogonal to $\boldsymbol{n}_0$ as well as to $\delta\boldsymbol{n}^{(1)}$. To evaluate the last two terms we need to project $\partial_x\delta\boldsymbol{n}^{(1)}$ on the plane orthogonal to $\boldsymbol{n}_0$, which is equal to $(\partial_x\chi_1 + A_x\chi_2)\boldsymbol{e}_1 + (\partial_x\chi_2 - A_x\chi_1)\boldsymbol{e}_2$. Using this and Eq. (B2) we can write the second term in the above equation as

$$\boldsymbol{n}_0 \cdot (\partial_x\delta\boldsymbol{n}^{(1)} \times \partial_y\boldsymbol{n}_0)$$

$$= \begin{vmatrix} \partial_x\chi_1 + A_x\chi_2 & -c_{2x} \\ \partial_x\chi_2 - A_x\chi_1 & c_{1x} \end{vmatrix}$$

$$= c_{1x}(\partial_x\chi_1 + A_x\chi_2) + c_{2x}(\partial_x\chi_2 - A_x\chi_1). \tag{C5}$$

Similarly, once can also write the third term as

$$\boldsymbol{n}_0 \cdot (\partial_x\boldsymbol{n}_0 \times \partial_y\delta\boldsymbol{n}^{(1)})$$

$$= \begin{vmatrix} c_{1x} & \partial_y\chi_1 + A_y\chi_2 \\ c_{2x} & \partial_y\chi_2 - A_y\chi_1 \end{vmatrix}$$

$$= c_{1x}(\partial_y\chi_2 + A_y\chi_1) - c_{2x}(\partial_y\chi_1 + A_y\chi_2). \tag{C6}$$

Now, we can use Eq. (C3) to show that $(\partial_x\chi_1 + A_x\chi_2, \partial_x\chi_2 - A_x\chi_1)^T$ and $(\partial_y\chi_1 + A_y\chi_2, \partial_y\chi_2 - A_y\chi_1)^T$ transform like $(\chi_1, \chi_2)^T$. This ensures the gauge invariance of Eqs. (C5) and (C6), since the determinant between two column vectors is invariant under rotations. Hence, this also ensures the gauge invariance of the δQ term in the energy functional

APPENDIX D: GAUGE-FIXING PROCEDURE

To mirror the problem of the experimentally relevant situation of a skyrmion crystal sandwiched between two ferromagnets, our heuristic model has to comprise a junction with zero vector potential on either side with a finite and varying vector potential in the central region. The heuristic model Hamiltonian with a finite and modulating magnetic field in the central region induces a vector potential, which increases from zero to a nonzero finite value. However, one can make a gauge transformation to ensure that the vector potential vanishes in the both the ends. In the Landau gauge

$$\tilde{A}_y(x, y) = \int_{-\infty}^{x} B(x', y)dx', \quad \tilde{A}_x = 0, \tag{D1}$$

while this vector potential has the same periodicity in y as the magnetic field, $A_y(\infty, y) \neq 0$ and is also dependent on y. One can fix this, while keeping the same $y-$ period $a/2$ of the magnetic field, provided the total flux within an infinite strip along x of width $a/2$ along y is an integer p (in units of the flux quantum). Such a procedure is only required for the heuristic model and not the actual skyrmion crystal problem, since in the latter we can choose local frames $\boldsymbol{e}_{1,2}(\boldsymbol{r})$ such that the associated vector potential vanishes far away from interfaces inside both ferromagnetic regions. We also note that in a skyrmion crystal the condition for integer units of flux quantum within an infinite strip of half period is satisfied.

For the procedure, we introduce the following notations for the lattice discretization of the problem. We define the magnetic field associated with a plaquette as

$$B(x, y) \equiv A_x(x, y) + A_y(x + 1, y) - A_x(x, y + 1) - A_y(x, y), \tag{D2}$$

where $A_{(x/y)}$ is the vector field along the $\hat{x}/\hat{y}$ direction on the link originating from the lattice point (x, y) [refer to Fig. 10(b) for sign convention]. Now, we put flux tubes each carrying flux -1 at $x = x_0$ and $y = y_i + ma/2$, with $0 \leqslant y_1 < y_2 < \ldots < y_p \leqslant a/2 - 1$, x_0 the midpoint of the central region and m an arbitrary integer. This singular flux configuration is described by the vector potential

$$\delta A_x(x, y) = 0, \quad x \neq x_0,$$

$$\delta A_y(x, y) = 0, \quad x \leqslant x_0,$$

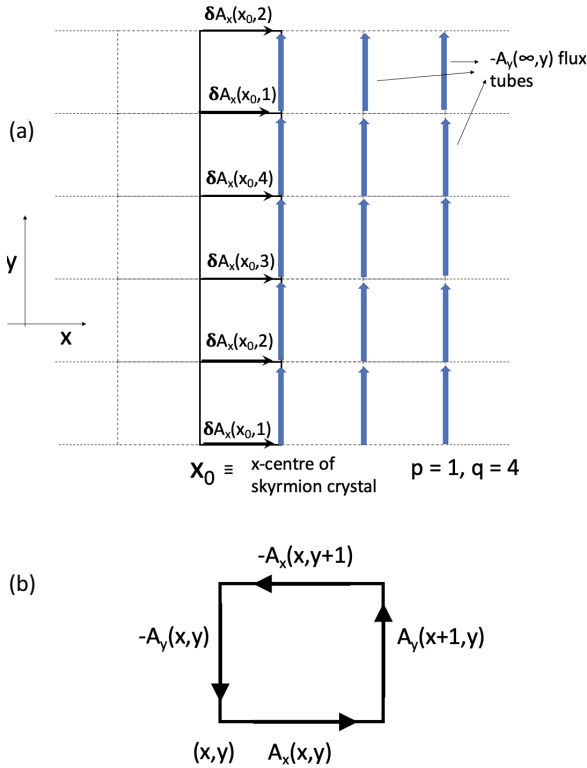$$\delta A_y(x, y) = -A_y(\infty, y), \quad x \geqslant x_0 + 1. \tag{D3}$$

FIG. 10. Gauge fixing procedure to ensure zero vector potential in the left and right ends. (a) Illustration of the procedure explained in this section for the case $p = 1, q = 4$. (b) Sign convention and notation for components of vector potential.

The condition on fluxes reads

$$\delta A_x(x_0, y) - \delta A_x(x_0, y + 1) - A_y(\infty, y)$$
$$= -\sum_{i=1} p \sum_m \delta_{y, y_i + mq}. \qquad \text{(D4)}$$

Starting from an arbitrary $\delta A_x(x_0, y)$, these equations determine successively $\delta A_x(x_0, y \pm 1), \delta A_x(x_0, y \pm 2)$ and so on. See Fig. 10(a) for a pictorial description of the flux addition procedure.

APPENDIX E: MULTICHANNEL SCATTERING—ROLE OF INTERFERENCE

To understand the role of interference between channels, for simplicity, we will consider a 1D system with coordinate x and N internal states (transverse positions, for example). Consider N-component wave functions $\Psi(x) \in \mathcal{C}^N$, subjected to the Hamiltonian

$$H = \tfrac{1}{2}(\overrightarrow{\partial_x} + iA(x))M^{-1}(x)(\overrightarrow{\partial_x} + iA(x)) + V(x), \qquad \text{(E1)}$$

where $M(x)$ is a positive definite, real and symmetric $N \times N$ matrix, a space-dependent effective mass. $V(x) = V^\dagger(x)$ plays the role of a local potential together with "hopping terms" in the transverse direction. Then $A(x) = A^\dagger(x)$ encodes an orbital generalized magnetic field.

Let Ψ satisfy $H\Psi = E\Psi$ with $E \in \mathbb{R}$. Then, we have a current $J(x) = \frac{1}{2i}(\Psi^\dagger(x)M^{-1}(x)(\overrightarrow{\partial_x} + iA)\Psi(x) - \Psi^\dagger(x)(\overleftarrow{\partial_x} - iA)M^{-1}(x)\Psi(x))$, which is independent of x.

The Schrödinger equation $H\psi = E\psi$ is linear and second order in $\frac{d}{dx}$, therefore it has a $2N$-dimensional space of solutions. For any point x, a solution is uniquely determined by specifying $\Psi(x)$ and $\frac{d\Psi(x)}{dx}$ in $\mathbb{C}^N$. The current $J(x)$ may be seen as a Hermitian form

$$J = \frac{1}{2}(\psi^\dagger \quad \psi^\dagger(\overleftarrow{\partial_x} - iA))$$
$$\times \begin{pmatrix} 0 & -iM^{-1} \\ iM^{-1} & 0 \end{pmatrix} \begin{pmatrix} \psi \\ (\overrightarrow{\partial_x} + iA)\psi \end{pmatrix}. \qquad \text{(E2)}$$

The linear map $(\psi, \partial_x\psi)^T \rightarrow (\psi, (\partial_x + iA)\psi)^T$ is one-to-one, so as a Hermitian form, J has the same signature as the middle matrix in the above equation. In a basis where M^{-1} is diagonal, we see that the eigenvalues of the matrix are $\pm m_1, ..., \pm m_N$, where $m_i > 0$ for $1 \leqslant i \leqslant N$. So we get the important result that the signature of J is of the type (N, N), at every point, independently of possible spatial variations of $M(x)$ and $A(x)$.

For a translationally invariant medium, we can look for plane-wave solutions $\psi(x) = e^{ikx}\psi$, with $k \in \mathbb{C}$. $\psi \in \mathbb{C}^N$ satisfies the eigenvalue equation

$$\tfrac{1}{2}(k\mathbb{1}^N + A)M^{-1}(k\mathbb{1}^N + A)\psi + V\psi = E\psi. \qquad \text{(E3)}$$

Let us consider the current carried by such eigenstates. Since the current is conserved, it vanishes unless the wavevector is real. However, we can also get a finite current from evanescent modes if we take linear superpositions $\psi(x) = e^{ik_1x}\psi_1 + e^{ik_2x}\psi_2$ when $k_1 = k_2^*$. Since J has signature (N, N), we have $2p$ propagating modes ($0 \leqslant p \leqslant N$), with p carrying a positive current and the other p carrying a negative current. The remaining $2(N - p)$ evanescent modes are grouped in pairs of modes with complex conjugate momenta.

The propagating modes with positive current have momenta $k_1, ..., k_p$, and those with negative current have momenta $k'_1, ..., k'_p$. In a time-reversal invariant effective medium (as it is the case when the vector potential vanishes), it is possible to label these momenta so that $k_j + k'_j = 0$. But in the presence of a nonzero vector potential, as inside a skyrmion crystal, there is no simple relation between the sets of k_j and of k'_j values. For evanescent modes, the corresponding momenta form pairs (k_j, k'_j) with $k'_j = k_j^*$ for $p + 1 \leqslant j \leqslant N$. We shall always assume that $\Im(k_j) > 0$ for such modes.

A general scattering solution at energy E can then be written in terms of $2N$ complex amplitudes A_j, B_j where $1 \leqslant j \leqslant N$ as

$$\psi(x) = \sum_{j=1}^N A_j e^{ik_jx}\psi_j + \sum_{j=1}^N B_j e^{k'_jx}\psi'_j. \qquad \text{(E4)}$$

It is possible to normalize the eigenstates ψ_j, ψ'_j such that

$$(\psi_j, J\psi_j) = 1 = -(\psi'_j, J\psi'_j); 1 \leqslant j \leqslant p,$$
$$(\psi'_j, J\psi_j) = 1 = (\psi_j, J\psi'_j); p + 1 \leqslant j \leqslant N, \qquad \text{(E5)}$$
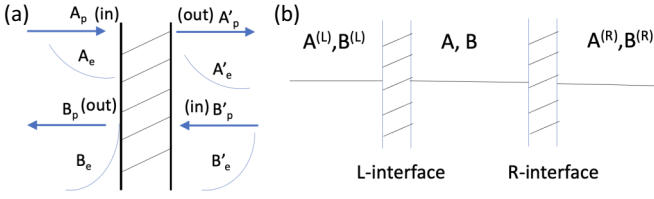
FIG. 11. Incoming and outgoing amplitudes for (a) a single interface problem and (b) a double interface problem.

and all other bilinears vanish. Then, using this normalization one gets

$$(\psi, J\psi) = \sum_{j=1}^{p}(|A_j|^2 - |B_j|^2) + \sum_{j=p+1}^{N}(A_j^* B_j + B_j^* A_j). \quad (E6)$$

Let us first consider the problem of a single interface as shown in Fig. 11(a). While the sign of the current determines the incoming and outgoing waves for the propagating channels, for evanescent channels we choose the waves, which decay towards the interface as incoming and the ones, which decay away from the interface as outgoing. The scattering matrix is then defined as

$$\begin{pmatrix} A'_p \\ A'_e \end{pmatrix} = \begin{pmatrix} t_{pp} & t_{pe} \\ t_{ep} & t_{pp} \end{pmatrix}\begin{pmatrix} A_p \\ A_e \end{pmatrix} + \begin{pmatrix} r'_{pp} & r'_{pe} \\ r'_{ep} & r'_{ee} \end{pmatrix}\begin{pmatrix} B'_p \\ B'_e \end{pmatrix},$$

$$\begin{pmatrix} B_p \\ B_e \end{pmatrix} = \begin{pmatrix} r_{pp} & r_{pe} \\ r_{ep} & r_{pp} \end{pmatrix}\begin{pmatrix} A_p \\ A_e \end{pmatrix} + \begin{pmatrix} t'_{pp} & t'_{pe} \\ t'_{ep} & t'_{ee} \end{pmatrix}\begin{pmatrix} B'_p \\ B'_e \end{pmatrix}. \quad (E7)$$

Imposing $(\psi, J\psi) = (\psi', J'\psi')$ for any choice of incoming amplitudes and using Eq. (E6) gives the unitarity relations,

$$t_{pp}^\dagger t_{pp} + r_{pp}^\dagger r_{pp} = \mathbb{1},$$
$$t_{pe}^\dagger t_{pp} + r_{pe}^\dagger r_{pp} = r_{ep}, \quad (E8)$$
$$t_{pe}^\dagger t_{pe} + r_{pe}^\dagger r_{pe} = r_{ee} + r_{ee}^\dagger,$$
$$t_{pp}^\dagger r'_{pp} + r_{pp}^\dagger t'_{pp} = 0,$$
$$t_{pe}^\dagger r'_{pp} + r_{pe}^\dagger t'_{pp} = t'_{ep},$$
$$t_{pp}^\dagger r'_{pe} + r_{pp}^\dagger t'_{pe} = -t_{ep}^\dagger,$$
$$t_{pe}^\dagger r'_{pe} + r_{pe}^\dagger t'_{pe} = t'_{ee} - t_{ee}^\dagger. \quad (E9)$$

For the relevant problem of two interfaces [Fig. 11(b)], one can write down a composition rule. To keep track of the distance L between the two interfaces we write Ae^{ikx} as $Ae^{ikL}e^{ik(x-L)}$. We may write

$$\begin{pmatrix} e^{ik^{(r)}L}A^{(r)} \\ e^{ik'L}B \end{pmatrix} = \begin{pmatrix} t^{(r)} & r'^{(r)} \\ r^{(r)} & t'^{(r)} \end{pmatrix}\begin{pmatrix} e^{ikL}A \\ e^{ik'^{(r)}L}B^{(r)} \end{pmatrix}. \quad (E10)$$

In particular $B = e^{-ik'L}r^{(r)}e^{ikL}A = r^{(r)}(L)A$, if $B^{(r)} = 0$. Our choice $\Im(k_j) > 0$ and $\Im(k'_j) = -\Im(k_j) < 0$ for evanescent channels ensures that $r_{pe}^{(r)}(L)$, $r_{ep}^{(r)}(L)$, and $r_{ee}^{(r)}(L)$ decay exponentially with L. This is also the case for $t_{pe}^{(r)}(L)$ whereas $t_{pp}^{(r)}(L)$ oscillates with L.

The general composition law reads

$$t = t^{(r)}(L)(\mathbb{1} - r'^{(l)}r^{(r)}(L))^{-1}t^{(l)}. \quad (E11)$$

In the limit where $L\Im(k_j) \gg 1$ for all $p + 1 \leqslant j \leqslant N$, we get for large L,

$$t \approx t^{(r)}(L)\Pi_p(\mathbb{1} - r'^{(l)}_{pp}r^{(r)}_{pp}(L))^{-1}\Pi_p t^{(l)}, \quad (E12)$$

where we have introduced the rank p projector Π_p on the subset of propagating channels inside the intermediate region. From the above equation we can directly see that if $p = 0$, i.e., all channels are evanescent, in the large L limit, there is no transmission. Moreover, if there is only one propagating channel, $p = 1$, and $|r_{pp}^{(l)}|$ and $|r_{pp}^{(r)}|$ are close to 1, sharp resonances with maximal transmission are possible. However, when $p \geqslant 2$, interference between the various propagating channels in the intermediate region decreases the maximal transmission at resonances.

To illustrate this point further, we note that the unitary relations (E8) and (E9) imply that the scattering submatrix S_{pp} associated to an interface and defined by

$$S_{pp} = \begin{pmatrix} r_{pp} & t'_{pp} \\ t_{pp} & r'_{pp} \end{pmatrix} \quad (E13)$$

is unitary.

From Eq. (E12), we see that resonances may occur when $t_{pp}^{(l)}$ and $t_{pp}^{(r)}$ are small. When t is small, we can write a unitary scattering matrix as

$$S \cong \begin{pmatrix} r_0(\mathbb{1} - \frac{1}{2}t^\dagger t) & -r_0 t^\dagger r'_0 \\ t & (\mathbb{1} - \frac{1}{2}tt^\dagger)r'_0 \end{pmatrix}, \quad (E14)$$

where r_0 and r'_0 are unitary matrices and all entries of t are small of order ϵ. Then $S^\dagger S = \mathbb{1} + O(\epsilon^3)$. Using this parametrization for $S_{pp}^{(l)}$ and $S_{pp}^{(r)}$ and dropping the pp subscript for notational convenience, Eq. (E12) becomes

$$t \cong t^{(r)}e^{ikL}(\mathbb{1} - (\mathbb{1} - t^{(l)}t^{\dagger(l)}/2)r'^{(l)}_0 e^{-ik'L}r^{(r)}_0$$
$$\times (\mathbb{1} - \frac{1}{2}t^{\dagger(r)}t^{(r)})e^{ikL})^{-1}t^{(L)}. \quad (E15)$$

So, the condition for resonance now selects the energies at which the unitary matrix $r'^{(l)}_0 e^{-ik'(E)L}r^{(r)}_0 e^{ik(E)L}$ has an eigenvalue equal to 1. When the number of propagating channels is at least two, we expect that the behavior of the transmission near these resonances is going to be significantly more complex than for a single propagating channel.

APPENDIX F: TIGHT-BINDING MODEL AND FORMS OF THE MATRIX ELEMENTS

In the main text we saw that the Schrödinger equation could be expressed as a tight-binding equation relating the wavefunctions of a slice to those to its left and right. On discretizing the energy functional and then taking the derivative we get a tight-binding problem with nearest- and next-nearest-neighbor hoppings. In this section we give illustrative examples of how the matrix elements for the matrices relating the different slices look. The nearest and next-nearest neighbor from the right contributions will enter as matrix elements in the A_R matrix, similar contributions from the left will enter in the A_L matrix and on-site contributions and nearest-neighbor contributions from above and below will enter in the D matrix. Let us look at some of the forms of these matrix elements.

First consider the exchange term. One can discretize this term by simply writing the contribution from the ith site as

$$E_{Ji} = J(\boldsymbol{n}_i - \boldsymbol{n}_{i+1})^2, \tag{F1}$$

expanding the above equation we get constants plus an $\boldsymbol{n}_i \cdot \boldsymbol{n}_{i+1}$ term. One can expand this term by expressing the $\boldsymbol{n}_i$ in terms of χ_1 and χ_2 by using Eqs. (A1) and (A2) in Appendix A. On doing so, and keeping up to $O(\chi_{1/2}^2)$ terms one finds that

$$\frac{\partial E_{ji}}{\partial \chi_{1i}} = \boldsymbol{n}_{0i} \cdot \boldsymbol{n}_{0j}\chi_{1i} - \boldsymbol{e}_{1i} \cdot (\chi_{1j}\boldsymbol{e}_{1j} + \chi_{2j}\boldsymbol{e}_{2j}), \tag{F2}$$

$$\frac{\partial E_{ji}}{\partial \chi_{2i}} = \boldsymbol{n}_{0i} \cdot \boldsymbol{n}_{0j}\chi_{2i} - \boldsymbol{e}_{2i} \cdot (\chi_{1j}\boldsymbol{e}_{1j} + \chi_{2j}\boldsymbol{e}_{2j}). \tag{F3}$$

From the above two equations one can directly read out the nearest-neighbor and on-site contributions from the coefficients of $\chi_{1/2j}$ and $\chi_{1/2i}$ respectively. The exchange term does not induce next-nearest-neighbor hopping. Now, after discretizing the topological charge terms as in the main text, we obtained a tight-binding model with hopping terms up to second-nearest neighbors. Let us consider one term from the first line in Eq. (22) of the main text. The derivative of this term can be expressed as

$$\frac{\partial \delta \Omega_{01}^2}{\partial \chi_{10}} = 2\delta \Omega_{01} \frac{\partial \delta \Omega_{01}}{\partial \chi_{10}}$$
$$= 2\delta \Omega_{01}\big(-f_{\alpha_{01}}\boldsymbol{z}_{01} \cdot \boldsymbol{e}_{10}\big), \tag{F4}$$

where $f_{\alpha_{01}} = \sin(\alpha_{01})/(1 + \cos(\alpha_{01}))$, and $\boldsymbol{n}_0 \times \boldsymbol{n}_1 = \sin(\alpha_{01})\boldsymbol{z}_{01}$. One can then expand $\delta \Omega_{01}$ using Eq. (20) in the main text, and then read off the coefficients same as above. A similar procedure can be used for all the other terms in Eq. (22).

APPENDIX G: SCALING FUNCTIONS FOR DISCRETIZATION

The real-space discretization procedure outlined in the main text requires each coupling constant to be scaled by a factor, so that the results are independent of N is the large N limit.

From the standard finite-difference type discretization scheme for the exchange terms, we know that the denominator will be $(a/N)^2$ because of the double derivative, where a/N is the grid size. Therefore, to get the correct continuum limit J should be multiplied by $(N/a)^2$. Similarly from the expression of the topological charge density, we can see that the denominator will be $(a/N)^4$, hence g should be multiplied by $(N/a)^4$.

While the argument above for the exchange term is pretty well known, the argument for the scaling of the g term might be a bit too simplistic. In which case one can also come up with a more sophisticated argument with the same result. Let us denote the topological charge of the $\boldsymbol{n}_0$ field generated by the theta functions in Sec. III, over a plaquette, to be $Q_\square$. If we change $\boldsymbol{n}_0$ to $\boldsymbol{n}_0 + \boldsymbol{n}_1$, where $\boldsymbol{n}_1$ is some small deviation such that $\boldsymbol{n}_0 \cdot \boldsymbol{n}_1 = 0$ everywhere, $Q_\square$ is changed into $Q_\square + \triangle Q_\square$, where

$$\triangle Q_\square = \frac{1}{4\pi} \oint \boldsymbol{n}_0 \cdot \left(\boldsymbol{n}_1 \times \frac{\partial \boldsymbol{n}_0}{\partial u}\right) du. \tag{G1}$$

Here, the integral is taken along the boundary of the above square plaquette and u is an arbitrary parameter on this boundary. It is convenient to write $\boldsymbol{n}_1 = \boldsymbol{v}(\boldsymbol{r}) \times \boldsymbol{n}_0(\boldsymbol{r})$, where $\boldsymbol{v}(\boldsymbol{r})$ is an infinitesimal rotation vector. Using the fact that $\boldsymbol{n}_0 \cdot \partial \boldsymbol{n}_0/\partial u = 0$, we get

$$\triangle Q_\square = \frac{1}{4\pi} \oint \boldsymbol{v} \cdot \frac{\partial \boldsymbol{n}_0}{\partial u} du. \tag{G2}$$

Using Green's equation one can express the above as an integral over the whole plaquette as

$$\triangle Q_\square = \frac{1}{4\pi} \iint_\square dx\, dy \left(\frac{\partial \boldsymbol{v}}{\partial x} \cdot \frac{\partial \boldsymbol{v}}{\partial y} - \frac{\partial \boldsymbol{v}}{\partial y} \cdot \frac{\partial \boldsymbol{n}_0}{\partial x}\right). \tag{G3}$$

As in the next section we check that if v is constant in space (global rotation in spin space), $\triangle Q_0 = 0$. Also, we see that $\triangle Q_\square$ is expected to be proportional to the plaquette area $(a/N)^2$, when N is large and $\boldsymbol{n}_0$ and $\boldsymbol{v}$ are smooth fields. Therefore, we may write

$$\triangle Q_\square = \delta\rho (a/N)^2, \tag{G4}$$

with $\delta\rho$ being the variation of the local topological charge density. Therefore, the first term in Eq. (A4) should scale as (in the large N limit, which is the relevant limit for numerics)

$$g \int (\delta\rho)^2 dx\, dy \approx g \sum_{\text{plaq}} \left[\triangle Q_\square\left(\frac{N^2}{a}\right)\right]^2 \left(\frac{a}{N}\right)^2$$
$$\approx g' \sum_{\text{plaq}} (\triangle Q_\square)^2 \left(\frac{a}{N}\right)^2. \tag{G5}$$

Hence, we see that the scaled version should be $g' = g(N/a)^4$

APPENDIX H: TEST FOR TOPOLOGICAL CHARGE DISCRETIZATION SCHEME

To test whether our geodesic scheme for discretizing the topological charge density is correct, we perform the following nontrivial check. As in the last section we take an infinitesimal rotation vector $\boldsymbol{v}$, constant in space, and rotate the ground-state spin vector $\boldsymbol{n}_0(\boldsymbol{r})$. On doing so, we can define new variables χ_1' and χ_2', which are related to the old variables by

$$\chi_1'(\boldsymbol{r}) = \boldsymbol{v} \cdot \boldsymbol{e}_2(\boldsymbol{r}),$$
$$\chi_2'(\boldsymbol{r}) = -\boldsymbol{v} \cdot \boldsymbol{e}_1(\boldsymbol{r}). \tag{H1}$$

Using the above expressions we form a column vector of the $\chi'(\boldsymbol{r}) = \chi_1'(\boldsymbol{r}) + i\chi_2'(\boldsymbol{r})$ and $\bar{\chi}'(\boldsymbol{r}) = \chi_1'(\boldsymbol{r})(\boldsymbol{r}) - i\chi_2'(\boldsymbol{r})$ from all the sites. We then right multiply the Hamiltonian constructed from only the topological charge density term ($J = 0$) and multiply it with this vector. If the discretization scheme is correct, then this product should be zero, since an infinitesimal global rotation should not induce any variation of the topological charge density. We have checked this in our calculations and indeed it does return a column of values, which are for all intents and purposes zero [$O(1e - 16)$].

TABLE I. Different properties of the bulk in the ferromagnet and skyrmion crystal highlighting the different order parameter manifolds. The most general form of coupling between these two that respects the individual properties shown in this table are given in Eqs. (J7) and (J11).

Property	Ferromagnet	Skyrmion crystal
Number of zero-energy deformations	2	3
Ground-state manifold	Sphere $\boldsymbol{n} \cdot \boldsymbol{n} = 1$	SO(3) group parameterized by x_1, x_2, x_3
Total angular momentum on ground-state manifold	$\boldsymbol{L} \sim \boldsymbol{n} \neq 0$	$\boldsymbol{L} = 0, (\pi_1, \pi_2, \pi_3 = 0)$
Dynamical variables	$\boldsymbol{n}$ with $\{n_i, n_j\} = \epsilon_{ijk}n_k$; $1 \leqslant n_i, n_j, n_k \leqslant 3$	$x_1, x_2, x_3, \pi_1, \pi_2, \pi_3$; $\{x_i, x_j\} = \{\pi_i, \pi_j\} = 0$; $\{x_i, \pi_j\} = \delta_{ij}$

APPENDIX I: BOUNDARY CONDITIONS FOR SPECTRA AND RELATION BETWEEN χ AND $\bar{\chi}$

To obtain the spectra of the skyrmion crystal, we considered periodic boundary conditions along both x and y axes of an $a \times a$ unit cell. For the tight-binding model after taking the derivative of the discretized energy functional, this implies that the for the right(left)-most site, the right(left)-nearest-neighbor contribution will pick up a $e^{iq_x a}(e^{-iq_x a})$ phase factor and similarly for the top(bottom)-most site, the top(bottom)-nearest-neighbor contribution will pick up a $e^{iq_y a}(e^{-iq_y a})$ phase factor. The phase factors encode how the momentum dependence enters the Hamiltonian matrix. The Hamiltonian is constructed in the site basis, so if there are N rows and columns each in the unit cell, the Hamiltonian has a size $2N^2 \times 2N^2$, where the factor of 2 comes because of the presence of both χ and $\bar{\chi}$. Each diagonal $2N \times 2N$ block of the Hamiltonian comprises the on-site, right- and left-nearest-neighbor contributions that come from that particular row. The off-diagonal blocks comprise the up- and down-nearest-neighbor terms as well as the second-nearest-neighbor contributions.

An important point to note while doing these calculations for the spectra and the scattering problem is that χ and $\bar{\chi}$ are not always complex conjugates of one another. To see this remember that from Appendix A, $\chi = \chi_1 + i\chi_2$ and $\bar{\chi} = \chi_1 - i\chi_2$; however, both χ_1 and χ_2 pickup complex phase factors $e^{\pm iq_{x/y}a}$ due to the boundary conditions as described above. For $q_x, q_y = 0$, the relation $\chi = \bar{\chi}^*$ holds since χ_1 and χ_2 are real. However, generally, this is not the case, since $\chi_1, \chi_2 \in \mathbb{C}$, and so $\chi \neq \bar{\chi}^*$.

APPENDIX J: COUPLING BETWEEN GOLDTSONE MODES—RECIPE FOR A NONLINEAR SIGMA MODEL

On top of the microscopic numerical calculations of the scattering problem, facilitated by the earlier developments, it is desirable to have a long-wavelength description for such junctions. Such a construction provides an analytical coarse-grained framework without delving into the specifics of the microscopic structure. These coarse-grained constructions usually take the form of nonlinear sigma models in magnetic systems. However, the construction of such a nonlinear sigma model for our problem is complicated by the presence of coupling between the ferromagnet and the skyrmion crystal at the interface, since both have different order parameter manifolds (see Table I). To understand what kind of couplings may arise at the interface of such a junction, one has to first construct a good parametrization of SO(3) to express the total angular momentum L in the x_i, π_j variables (see Table I). Such a parametrization will allow us to construct SO(3) invariant Hamiltonians in the vicinity of the degenerate ground-state manifold of the noncollinear skyrmion crystal, and will help us find ways to couple it to $\boldsymbol{n}$ in an SO(3) invariant way.

We start by writing rotation matrices in terms of SU(2) matrices. Consider the family of such rotation matrices of the form

$$U(\boldsymbol{x}) = \begin{bmatrix} \sqrt{1 - \boldsymbol{x}^2} + ix_3 & ix_1 + x_2 \\ ix_1 - x_2 & \sqrt{1 - \boldsymbol{x}^2} - ix_3 \end{bmatrix}$$
$$= \sqrt{1 - \boldsymbol{x}^2}\mathbb{1} + i\boldsymbol{x} \cdot \boldsymbol{\sigma}. \quad \text{(J1)}$$

Since SO(3) is non-Abelian we have two distinct actions of SU(2) on itself, either by left or right multiplication. Note that any left multiplication commutes with any right multiplication, $U(VW) = (UV)W$; however, two left or two right multiplications do not commute. We choose left actions to correspond to global SO(3) symmetries, and generators of right actions therefore, to commute with generators of global symmetries—they can be used to construct effective low-energy Hamiltonians.

Let us first study the left action. Consider an infinitesimal rotation $\exp(-i\frac{\boldsymbol{\epsilon}}{2} \cdot \boldsymbol{\sigma})$ where $\boldsymbol{\epsilon}$ is a small vector in $\mathbb{R}^3$. Now,

$$\left(\mathbb{1} - i\frac{\boldsymbol{\epsilon}}{2} \cdot \boldsymbol{\sigma}\right)U(\boldsymbol{x}) = U(\boldsymbol{x} + X_\epsilon(\boldsymbol{x})) + O(\epsilon^2)$$
$$X_\epsilon(\boldsymbol{x}) = -\sqrt{1 - \boldsymbol{x}^2}\frac{\boldsymbol{\epsilon}}{2} + \frac{\boldsymbol{\epsilon} \times \boldsymbol{x}}{2}. \quad \text{(J2)}$$

When $\epsilon \to 0$, $X_\epsilon(\boldsymbol{x})$ may be seen as a tangent vector to the SO(3) group manifold at point $\boldsymbol{x}$, so $x \to X_\epsilon(\boldsymbol{x})$ is a vector field associated to the infinitesimal rotation.

Vector fields form a Lie algebra under the Lie bracket. We can check that $[X_\epsilon, X_\eta] = X_{\eta \times \epsilon}$, which is the Lie-algebra structure of SO(3) in $\mathbb{R}^3$ (see Appendix K for details). Now, coming to the right action of the rotation matrix, we find that

$$U(\boldsymbol{x})\left(\mathbb{1} + i\frac{\boldsymbol{\epsilon}}{2} \cdot \boldsymbol{\sigma}\right) = U(\boldsymbol{x} + Y_\epsilon(\boldsymbol{x})) + O(\epsilon^2)$$
$$Y_\epsilon(\boldsymbol{x}) = \sqrt{1 - \boldsymbol{x}^2}\frac{\boldsymbol{\epsilon}}{2} + \frac{\boldsymbol{\epsilon} \times \boldsymbol{x}}{2}. \quad \text{(J3)}$$

We can recover the same Lie-algebra structure as for the left action here as well.

In Hamiltonian mechanics, angular momentum defined by $\tilde{L} = \epsilon_{ijk} x_j \pi_k$ generates rotations in phase space owing to its commutation relations with the x and π variables. From the equations of X_ϵ and Y_ϵ, one can show that the left action is generated by $\epsilon \cdot L$ where

$$L_i = \tfrac{1}{2}(-\sqrt{1-x^2}\pi_i + \tilde{L}_i), \tag{J4}$$

and the right action is generated by $\epsilon \cdot R$, where

$$R_i = \tfrac{1}{2}(\sqrt{1-x^2}\pi_i + \tilde{L}_i). \tag{J5}$$

These functions satisfy the commutation relations $\{L_i, L_j\} = \epsilon_{ijk} L_k$, $\{R_i, R_j\} = \epsilon_{ijk} R_k$ and $\{L_i, R_j\} = 0$.

For the uniform ($q = 0$) sector, the noncollinear skyrmion crystal Hamiltonian contains only a kinetic term, which we take to be quadratic in the R_i variables, since $R_i = 0$ identically on the degenerate ground-state manifold and R_i deviates linearly from zero when π_i's are small. We can write this term as

$$H_K = \frac{1}{2}\sum_{a,b} I_{ab}^{-1} R_a R_b, \tag{J6}$$

where I_{ab} is a positive definite symmetric matrix with real entries, which may be regarded as a generalized inertia matrix for a kind of top.

The simplest left-invariant coupling between the ferromagnetic magnetization n and the skyrmion crystal system is given by

$$H_{c1} = g_c n \cdot L, \tag{J7}$$

where g_c is some coupling constant.

Since the coupling terms occur at the interface one can also consider coupling n to a fraction of the spins composing the skyrmion crystal (those belonging to the interface) in an SU(2) invariant way. So we should be able to construct triples of functions over the SU(2) group manifold (with x coordinates), which transform as the three components of the usual vectors under usual SO(3) rotations. To express this in the coordinates obtained for SU(2), we use the Heisenberg picture for observables. We set $\sigma(x) \equiv U^\dagger(x)\sigma U(x)$. Now, let us change x to $x + X_{a'}$, where a' is an infinitesimal vector. By construction, this amounts to sending $U(x)$ to $\exp(-i\frac{a'}{2} \cdot \sigma)U(x)$. Using the above and the relations $[\sigma_i, \sigma_j] = 2i\epsilon_{ijk}\sigma_k$ and $[a' \cdot \sigma, \sigma] = -2ia' \times \sigma$, one gets that

$$\sigma(x + X_{a'}) = \sigma(x) + a' \times \sigma(x) + O(a'^2). \tag{J8}$$

We can then choose any density matrix ρ_0 (with $\rho = \rho^\dagger$, positive eigenvalues and $\mathrm{Tr}\rho_0 = 1$) and form a vector-valued function

$$\langle \sigma \rangle_{\rho_0} : \mathrm{SU}(2) \to \mathbb{R}^3,$$
$$U(x) \to \langle \sigma \rangle_{\rho_0} \equiv \mathrm{Tr}(\sigma(x)\rho_0). \tag{J9}$$

Then, Eq. (J8) implies that

$$\langle \sigma(x + X_a) \rangle_{\rho_0} = \langle \sigma(x) \rangle_{\rho_0} + a \times \langle \sigma(x) \rangle_{\rho_0}. \tag{J10}$$

Hence, one can write down a second kind of coupling term

$$H_{c2} = g_c' n \cdot \langle \sigma(x) \rangle_{\rho_0}, \tag{J11}$$

where g_c' is some other coupling constant. Therefore the full sigma model Hamiltonian including the standard gradient potential terms for the bulk would be

$$H_\sigma = H_{\mathrm{bulk}} + H_K + H_{c1} + H_{c2}, \tag{J12}$$

where the coupling terms would be evaluated at the coordinates of the interface. One can use this model to calculate the equations of motion and the corresponding transmission coefficients. Following this, one can fit the results to the values obtained numerically from our transfer matrix calculations to get the values of all the coupling constants in the sigma model. However, we leave a detailed analysis of such sigma models for future work.

APPENDIX K: LIE-ALGEBRA STRUCTURE IN NONLINEAR SIGMA MODEL

In this Appendix we give details on some of the calculations to show the Lie-algebra structure of the vector fields mentioned in Appendix J. We showed that $x \to X_{\epsilon(x)}$ is a vector field associated to the infinitesimal left rotation $\exp(-i\epsilon \cdot \sigma/2)$. We know that vector fields form a Lie algebra under the Lie bracket. The Lie bracket is defined as

$$L_{[X,Y]}(f) = (L_X L_Y - L_Y L_X)f \tag{K1}$$

for any arbitrary function f, where $L_X f \equiv \sum_i X^i \partial_i f$ denotes the Lie derivative of f along vector field X. We can write the Lie derivative as

$$(L_X L_Y - L_Y L_X)f$$
$$= X^i \partial_i (Y^j \partial_j f) - Y^j \partial_j (X^i \partial_i f)$$
$$= (X^i \partial_i Y^j - Y^i \partial_i X^j)\partial_j f \equiv [X, Y]^j \partial_j f, \tag{K2}$$

therefore we get $[X, Y] = X \cdot \nabla Y - Y \cdot \nabla X \equiv Y'(X) - X'(Y)$ where X' denotes the Jacobian matrix $(X')_i^j \equiv \partial_i X^j$. Now, let us compute $[X_\epsilon, X_\eta]$. Using Eq. (J2) from the main text we can write

$$X'_\eta(X_\epsilon) = -\frac{x}{\sqrt{1-x^2}} \cdot \left(\sqrt{1-x^2}\frac{\epsilon}{2} - \frac{\epsilon}{2} \times x\right)\frac{\eta}{2}$$
$$- \frac{\eta}{2} \times \left(\sqrt{1-x^2}\frac{\epsilon}{2} - \frac{\epsilon}{2} \times x\right)$$
$$= -\frac{1}{4}((x \cdot \epsilon)\eta + \sqrt{1-x^2}\,\eta \times \epsilon - \eta \times (\epsilon \times x)). \tag{K3}$$

Similarly one can also write

$$X'_\epsilon(X_\eta) = -\frac{1}{4}((x \cdot \eta)\epsilon + \sqrt{1-x^2}\,\epsilon \times \eta - \epsilon \times (\eta \times x)). \tag{K4}$$

Using the above two equations one gets

$$[X_\epsilon, X_\eta] = \frac{1}{4}(((x \cdot \eta)\epsilon - (x \cdot \epsilon)\eta) + 2\sqrt{1-x^2}\epsilon \times \eta$$
$$- (\epsilon \times (\eta \times x) - \eta \times (\epsilon \times x)))$$

$$= \sqrt{1-x^2} \frac{\boldsymbol{\epsilon} \times \boldsymbol{\eta}}{2} - \frac{1}{2}(\boldsymbol{\epsilon} \times \boldsymbol{\eta}) \times \boldsymbol{x}$$

$$= X_{\boldsymbol{\eta} \times \boldsymbol{\epsilon}}, \tag{K5}$$

and, hence, we recover the Lie-algebra structure of SO(3). Similarly for the right action we get

$$[\boldsymbol{Y}_{\boldsymbol{\epsilon}}, \boldsymbol{Y}_{\boldsymbol{\eta}}] = -\boldsymbol{Y}_{\boldsymbol{\epsilon} \times \boldsymbol{\eta}} = \boldsymbol{Y}_{\boldsymbol{\eta} \times \boldsymbol{\epsilon}}. \tag{K6}$$

Let us examine the correspondence between Poisson brackets $\{g, h\}$ and Lie brackets $[X_g, X_h]$ of their associated Hamiltonian vector fields X_g and X_h. Hamilton's equations, relating X_g to g, are equivalent to requiring $L_{X_g} f = \{f, g\}$ for any function f over phase space. Then we have

that

$$L_{X_g} L_{X_h}(f) = \{\{f, h\}, g\},$$
$$L_{X_h} L_{X_g}(f) = \{\{f, g\}, h\}, \tag{K7}$$

hence, one can express the Lie bracket as

$$L_{[X_g, X_h]}(f) = \{\{f, h\}, g\} + \{\{g, f\}, h\} = -\{\{h, g\}, f\}$$

$$= \{f, \{h, g\}\} = L_{X_{\{h,g\}}}(f), \tag{K8}$$

$$[X_g, X_h] = X_{\{h,g\}},$$

where in the second equality of the first line in the above equation we have used the Jacobi identity.

[1] P. W. Anderson, *Basic Notions of Condensed Matter Physics* (CRC Press, Boca Raton, FL, 2018)

[2] R. Moessner and J. E. Moore, *Topological Phases of Matter* (Cambridge University Press, Cambridge, 2021).

[3] S. L. Sondhi, A. Karlhede, S. A. Kivelson, and E. H. Rezayi, Phys. Rev. B **47**, 16419 (1993).

[4] L. Brey, H. A. Fertig, R. Côté, and A. H. MacDonald, Phys. Rev. Lett. **75**, 2562 (1995).

[5] R. Rajaraman, *Solitons and Instantons: An Introduction to Solitons and Instantons in Quantum Field Theory* (Elsevier, Amsterdam, 1982).

[6] S. Mühlbauer, B. Binz, F. Jonietz, C. Pfleiderer, A. Rosch, A. Neubauer, R. Georgii, and P. Böni, Science **323**, 915 (2009).

[7] X. Yu, Y. Onose, N. Kanazawa, J. H. Park, J. Han, Y. Matsui, N. Nagaosa, and Y. Tokura, Nature (London) **465**, 901 (2010).

[8] G. Gervais, H. L. Stormer, D. C. Tsui, P. L. Kuhns, W. G. Moulton, A. P. Reyes, L. N. Pfeiffer, K. W. Baldwin, and K. W. West, Phys. Rev. Lett. **94**, 196803 (2005).

[9] W. Desrat, D. K. Maude, M. Potemski, J. C. Portal, Z. R. Wasilewski, and G. Hill, Phys. Rev. Lett. **88**, 256807 (2002).

[10] V. Bayot, E. Grivei, S. Melinte, M. B. Santos, and M. Shayegan, Phys. Rev. Lett. **76**, 4584 (1996).

[11] Y. Gallais, J. Yan, A. Pinczuk, L. N. Pfeiffer, and K. W. West, Phys. Rev. Lett. **100**, 086806 (2008).

[12] H. Zhu, G. Sambandamurthy, Y. P. Chen, P. Jiang, L. W. Engel, D. C. Tsui, L. N. Pfeiffer, and K. W. West, Phys. Rev. Lett. **104**, 226801 (2010).

[13] D. S. Wei, T. Van Der Sar, S. H. Lee, K. Watanabe, T. Taniguchi, B. I. Halperin, and A. Yacoby, Science **362**, 229 (2018).

[14] T. X. Zhou, J. J. Carmiggelt, L. M. Gächter, I. Esterlis, D. Sels, R. J. Stöhr, C. Du, D. Fernandez, J. F. Rodriguez-Nieva, F. Büttner *et al.*, Proc. Natl. Acad. Sci. USA **118**, e2019473118 (2021).

[15] H. Zhou, C. Huang, N. Wei, T. Taniguchi, K. Watanabe, M. P. Zaletel, Z. Papić, A. H. MacDonald, and A. F. Young, Phys. Rev. X **12**, 021060 (2022).

[16] A. T. Pierce, Y. Xie, S. H. Lee, P. R. Forrester, D. S. Wei, K. Watanabe, T. Taniguchi, B. I. Halperin, and A. Yacoby, Nat. Phys. **18**, 37 (2022).

[17] A. Assouline, M. Jo, P. Brasseur, K. Watanabe, T. Taniguchi, T. Jolicoeur, D. Glattli, N. Kumada, P. Roche, F. Parmentier *et al.*, Nat. Phys. **17**, 1369 (2021).

[18] Y. Zhang, Y.-W. Tan, H. L. Stormer, and P. Kim, Nature (London) **438**, 201 (2005).

[19] K. S. Novoselov, Z. Jiang, Y. Zhang, S. Morozov, H. L. Stormer, U. Zeitler, J. Maan, G. Boebinger, P. Kim, and A. K. Geim, Science **315**, 1379 (2007).

[20] S. M. Girvin, *Aspects topologiques de la physique en basse dimension, Topological aspects of low dimensional systems, Les Houches - Ecole d'Ete de Physique Theorique*, Vol. 69, edited by A. Comtet, T. Jolicur, S. Ouvry, and F. David (Springer, Berlin, Heidelberg, 2002), pp. 537–175.

[21] M. Z. Hasan and C. L. Kane, Rev. Mod. Phys. **82**, 3045 (2010).

[22] H. Zhou, H. Polshyn, T. Taniguchi, K. Watanabe, and A. Young, Nat. Phys. **16**, 154 (2020).

[23] R. Côté, D. B. Boisvert, J. Bourassa, M. Boissonneault, and H. A. Fertig, Phys. Rev. B **76**, 125320 (2007).

[24] D. L. Kovrizhin, B. Douçot, and R. Moessner, Phys. Rev. Lett. **110**, 186802 (2013).

[25] J. Zang, M. Mostovoy, J. H. Han, and N. Nagaosa, Phys. Rev. Lett. **107**, 136804 (2011).

[26] O. Petrova and O. Tchernyshyov, Phys. Rev. B **84**, 214433 (2011).

[27] T. Weber, D. M. Fobes, J. Waizner, P. Steffens, G. Tucker, M. Bohm, L. Beddrich, C. Franz, H. Gabold, R. Bewley *et al.*, Science **375**, 1025 (2022).

[28] J. Iwasaki, A. J. Beekman, and N. Nagaosa, Phys. Rev. B **89**, 064412 (2014).

[29] C. Schütte and M. Garst, Phys. Rev. B **90**, 094423 (2014).

[30] S. Lee, K. Nakata, O. Tchernyshyov, and S. K. Kim, Phys. Rev. B **107**, 184432 (2023).

[31] N. Paul, Y. Zhang, and L. Fu, Sci. Adv. **9**, eabn1401 (2023).

[32] O. Debarre, *Complex Tori and Abelian Varieties* (American Mathematical Society, Providence, RI, 2005), Vol. 6.

[33] B. Douçot, M. O. Goerbig, P. Lederer, and R. Moessner, Phys. Rev. B **78**, 195327 (2008).

[34] J. Pendry, J. Mod. Opt. **41**, 209 (1994).

[35] J. Atteia, F. Parmentier, P. Roulleau, and M. O. Goerbig, arXiv:2204.12795.

[36] N. Wei, C. Huang, and A. H. MacDonald, Phys. Rev. Lett. **126**, 117203 (2021).

[37] K. Moon, H. Mori, K. Yang, S. M. Girvin, A. H. MacDonald, L. Zheng, D. Yoshioka, and S.-C. Zhang, Phys. Rev. B **51**, 5138 (1995).

[38] F. D. M. Haldane and E. H. Rezayi, Phys. Rev. B **31**, 2529 (1985).

[39] J.-L. Pichard and G. Sarma, J. Phys. C **14**, L617 (1981).

[40] A. MacKinnon and B. Kramer, Phys. Rev. Lett. **47**, 1546 (1981).

[41] D. S. Fisher and P. A. Lee, Phys. Rev. B **23**, 6851 (1981).

[42] B. Douçot, D. L. Kovrizhin, and R. Moessner, Ann. Phys. **399**, 239 (2018).

[43] M. Kharitonov, Phys. Rev. B **85**, 155439 (2012).

[44] M. Kim, S. Xu, A. Berdyugin, A. Principi, S. Slizovskiy, N. Xin, P. Kumaravadivel, W. Kuang, M. Hamer, R. Krishna Kumar *et al.*, Nat. Commun. **11**, 2339 (2020).

[45] H. A. Fertig, L. Brey, R. Côté, A. H. MacDonald, A. Karlhede, and S. L. Sondhi, Phys. Rev. B **55**, 10671 (1997).

[46] A. Coissard, A. G. Grushin, C. Repellin, L. Veyrat, K. Watanabe, T. Taniguchi, F. Gay, H. Courtois, H. Sellier, and B. Sacépé, Sci. Adv. **9**, eadf7220 (2023).

[47] Y. Cao, V. Fatemi, A. Demir, S. Fang, S. L. Tomarken, J. Y. Luo, J. D. Sanchez-Yamagishi, K. Watanabe, T. Taniguchi, E. Kaxiras *et al.*, Nature (London) **556**, 80 (2018).

[48] Y. Cao, V. Fatemi, S. Fang, K. Watanabe, T. Taniguchi, E. Kaxiras, and P. Jarillo-Herrero, Nature (London) **556**, 43 (2018).

[49] E. Khalaf, S. Chatterjee, N. Bultinck, M. P. Zaletel, and A. Vishwanath, Sci. Adv. **7**, eabf5299 (2021).

[50] E. Khalaf and A. Vishwanath, Nat. Commun. **13**, 6245 (2022).

[51] Y. H. Kwan, G. Wagner, N. Bultinck, S. H. Simon, and S. A. Parameswaran, Phys. Rev. X **12**, 031020 (2022).

[52] S. Chatterjee, N. Bultinck, and M. P. Zaletel, Phys. Rev. B **101**, 165141 (2020).

[53] S. Grover, M. Bocarsly, A. Uri, P. Stepanov, G. Di Battista, I. Roy, J. Xiao, A. Y. Meltzer, Y. Myasoedov, K. Pareek *et al.*, Nat. Phys. **18**, 885 (2022).

[54] Y. Xu, A. Ray, Y.-T. Shao, S. Jiang, D. Weber, J. E. Goldberger, K. Watanabe, T. Taniguchi, D. A. Muller, K. F. Mak *et al.*, arXiv:2103.09850.

[55] M. Akram, H. LaBollita, D. Dey, J. Kapeghian, O. Erten, and A. S. Botana, Nano Lett. **21**, 6633 (2021).

[56] L. Brey, H. A. Fertig, R. Côté, and A. H. MacDonald, Phys. Rev. B **54**, 16888 (1996).

[57] R. Kamilla, X. Wu, and J. Jain, Solid State Commun. **99**, 289 (1996).

[58] A. C. Balram, U. Wurstbauer, A. Wójs, A. Pinczuk, and J. Jain, Nat. Commun. **6**, 8981 (2015).

[59] R. L. Doretto, M. O. Goerbig, P. Lederer, A. O. Caldeira, and C. Morais Smith, Phys. Rev. B **72**, 035341 (2005).

[60] A. Wójs and J. J. Quinn, Phys. Rev. B **66**, 045323 (2002).

[61] Y. Lian and M. O. Goerbig, Phys. Rev. B **95**, 245428 (2017).

[62] P. Yan, X. S. Wang, and X. R. Wang, Phys. Rev. Lett. **107**, 177207 (2011).

[63] S. K. Kim, Y. Tserkovnyak, and O. Tchernyshyov, Phys. Rev. B **90**, 104406 (2014).

[64] L. Šmejkal, Y. Mokrousov, B. Yan, and A. H. MacDonald, Nat. Phys. **14**, 242 (2018).